PNAS RESEARCH ARTICLE | ENGINEERING

A flexible and highly sensitive organic electrochemical transistor-based biosensor for continuous and wireless nitric oxide detection

Yuping Deng[a,1], Hui Qi[b,1], Yuan Ma[c,1], Shangbin Liu[d,1], Mingyou Zhao[e], Zhenhu Guo[a,f], Yongsheng Jie[b], Rui Zheng[b], Jinzhu Jing[g], Kuntao Chen[a], He Ding[h], Guoqing Lv[h], Kaiyuan Zhang[i], Rongfeng Li[j], Huanyu Cheng[d], Lingyun Zhao[a], Xing Sheng (盛兴)[i], Milin Zhang[c,2], and Lan Yin (尹斓)[a,2]

Edited by John Rogers, Northwestern University, Evanston, IL; received May 10, 2022; accepted July 13, 2022

As nitric oxide (NO) plays significant roles in a variety of physiological processes, the capability for real-time and accurate detection of NO in live organisms is in great demand. Traditional assessments of NO rely on indirect colorimetric techniques or electrochemical sensors that often comprise rigid constituent materials and can hardly satisfy sensitivity and spatial resolution simultaneously. Here, we report a flexible and highly sensitive biosensor based on organic electrochemical transistors (OECTs) capable of continuous and wireless detection of NO in biological systems. By modifying the geometry of the active channel and the gate electrodes of OECTs, devices achieve optimum signal amplification of NO. The sensor exhibits a low response limit, a wide linear range, high sensitivity, and excellent selectivity, with a miniaturized active sensing region compared with a conventional electrochemical sensor. The device demonstrates continuous detection of the nanomolar range of NO in cultured cells for hours without significant signal drift. Real-time and wireless measurement of NO is accomplished for 8 d in the articular cavity of New Zealand White rabbits with anterior cruciate ligament (ACL) rupture injuries. The observed high level of NO is associated with the onset of osteoarthritis (OA) at the later stage. The proposed device platform could provide critical information for the early diagnosis of chronic diseases and timely medical intervention to optimize therapeutic efficacy.

nitric oxide sensor | organic electrochemical transistor | flexible electronics | osteoarthritis

Significance

Nitric oxide (NO) has demonstrated critical functions in biological systems, and strategies enabling continuous monitoring of NO are of tremendous interest for diagnostic and therapeutic applications. Here, we develop a flexible, wirelessly operated, and highly sensitive biosensor based on organic electrochemical transistors for the real-time detection of NO. Remarkable advances over conventional electrochemical sensors include a wide sensing range, a low response limit, high sensitivity, and miniaturized active sensing regions. Real-time and wireless monitoring of NO in the articular cavity over an 8-d period is accomplished, which could provide essential early diagnosis and preventive treatments of posttraumatic osteoarthritis progression. The work shows promise, offering a critical engineering basis for decoding health conditions at the early stage and maximizing therapeutic outcomes.

Nitric oxide (NO), as a highly labile signaling molecule produced in biological systems by nitric oxide synthases (NOSs), plays a significant role in regulating immune, cardiovascular, and nervous systems (1, 2). Under abnormal conditions, an excessive amount of NO works as a proinflammatory mediator and promotes inflammation; for example, increased release of NO has been associated with chondrocyte cell death and osteoarthritis (OA) (3, 4). NO could, therefore, potentially serve as a biomarker in the articular cavity for the early diagnosis of OA (5, 6). Anterior cruciate ligament (ACL) rupture is one of the most prevalent knee injuries and is often found in athletes. Twenty-nine of 100,000 people are estimated to suffer from ACL injuries, and costs up to $500 million are associated with treatments per year in the United States (7, 8). ACL tears and concomitant injuries are believed to be responsible for posttraumatic cartilage damage and the early onset of OA, probably due to abnormal mechanical loads in the knee joint and up-regulated inflammatory cytokines (9). Compared with conventional diagnostic techniques, such as radiographic imaging and medical assessment of patient symptoms, which often occur in the later stages of OA (10, 11), real-time assessment of associated biomarkers, such as NO in the joint cavity, could identify pathologic evolution at the initial phase and could, therefore, provide essential information to optimize therapies following traumatic knee injury and evaluate the risks of OA progression.

Previous studies have identified an increase in NO production resulting from the transection of the ACL (12, 13). However, the vast majority of techniques proposed in these studies are based on colorimetry, which relies on sensing secondary species, such as nitrite, with conventional Griess assays and is incapable of real-time monitoring. Other methods directly capturing NO, such as electron paramagnetic resonance spectroscopy, chemiluminescence, mass spectrometry, and fluorescence, are limited by their insufficient sensitivity as well as the requirement of complex sample preparation and an expensive experimental apparatus that impedes continuous detection (14–16). Electrochemical sensing based on a three-electrode configuration has the advantages of desirable sensitivity and selectivity, and a flexible and physically transient electrochemical sensor has recently been achieved for real-time NO detection in biological systems (17). However, it remains a challenge to simultaneously attain both high sensitivity

The authors declare no competing interest.

This article is a PNAS Direct Submission.

[1]Y.D., H.Q., Y.M. and S.L. contributed equally to this work.

[2]To whom correspondence may be addressed. Email: zhangmilin@tsinghua.edu.cn or lanyin@tsinghua.edu.cn.

This article contains supporting information online at http://www.pnas.org/lookup/suppl/doi:10.1073/pnas.2208060119/-/DCSupplemental.

Published August 16, 2022.

and high spatial resolution with electrochemical sensors because device sensitivity is often dependent on the electroactive surface area (18). In addition, the sensing stability of electrochemical sensors relies on the reference electrodes, and recalibration might be required on a regular basis to ensure desirable accuracy (19).

Transistor-based devices with signal amplification capability could potentially address the aforementioned issues (20, 21). In vitro NO detection with subnanomolar sensitivity has been reported using miniaturized hemin-functionalized graphene field-effect transistors (FETs) (22). Nevertheless, continuous NO detection in living organisms has rarely been investigated. As a high-performance transducer, organic electrochemical transistors (OECTs) serve as promising devices for the in vivo detection of critical biomarkers, with a high spatial resolution due to their facile processing, high sensitivity, and excellent biocompatibility and flexibility, which match the nature of biological systems (23, 24). Different from conventional FETs, OECTs have active channels in direct contact with an electrolyte. The conductivity of the channel is modulated by the gate voltage via electrochemical reactions that determine the injection of ions from the electrolyte into the channel, changing its doping state. As the doping process occurs in the entire volume of the channel of OECTs, the doping enables the amplification of electrochemical signals and therefore, significantly increases sensing sensitivity (25, 26). More intriguing, reference and counterelectrodes are not necessary in OECT systems compared with three-electrode electrochemical sensors, and miniaturization is thus possible without compromising the performance (27, 28).

Conducting polymer poly(3,4-ethylenedioxythiophene) (PEDOT): poly(styrene sulfonate) (PSS) represents a typical material for OECTs, in which holes serve as the charge carriers as PEDOT is p-type doped ($PEDOT^+$), and the sulfonate anions of PSS (PSS^-) can be considered as ionized acceptors (24). OECTs based on PEDOT:PSS work in depletion mode in the sense that the channel current decreases upon a positive gate bias and will eventually reach the off state with increasing gate voltages due to the injection of cations from the electrolyte to the channel compensating the sulfonate anions of PSS (24). Recent studies of OECTs based on PEDOT:PSS for biosensing are focused mostly on the detection of electrophysiological signals (23, 29, 30) or biomarkers, such as dopamine, glucose (GLU), lactate, and antibodies (31–36), where a relatively low gate voltage (<0.6 V) is applied. However, the detection of NO with PEDOT:PSS-based OECTs remains a challenge since the oxidation of NO occurs at high voltages (typically ≥0.8 V) that fall beyond the range of functional gate bias of PEDOT:PSS devices with conventional geometries, and transistors will reach the off state. As the operational characteristics of PEDOT:PSS-based OECTs have been shown to rely on gate materials and the aspect ratios of channels (37), advanced material strategies and device architectures are critical to take advantage of OECTs to accomplish real-time NO sensing with both high sensitivity and spatial resolution in biological environments.

Here, we develop flexible OECT-based biosensors integrated with a wireless module for real-time NO detection in the articular cavity (Fig. 1). By optimizing the geometrical structures of PEDOT:PSS-based OECTs, desirable performance is achieved for signal amplification for NO measurement, with miniaturized active regions compared with conventional electrochemical NO sensors. The device delivers a low response limit of 3 nM, a high sensitivity of 94 mV/dec, a wide linear range from 3 nM to 100 μM, and excellent selectivity over other substances, including GLU, sodium nitrite, sodium nitrate, ascorbic acid (AA), uric acid (UA), etc. Continuous measurement of NO in chondrocytes for a 10-h period has been demonstrated, and the results match the measurements collected with a standard Griess assay. Wireless and real-time monitoring of NO levels in the joint cavity of New Zealand rabbits after ACL rupture injuries is accomplished for 8 d. Relatively high NO concentrations are captured, which are associated with subsequent cartilage degeneration after 8 wk, indicating the onset of OA. The proposed materials and devices enable robust tools for monitoring NO wirelessly and continuously in biological systems and could potentially provide vital information for early-stage diagnosis and therapy optimization, which are beneficial for health care.

Results

Material Schemes and Device Fabrication of NO Sensors. The NO sensor based on OECTs consists of a PEDOT:PSS channel with source, drain, and gate electrodes; a selective membrane (poly-5-amino-1-naphthol [poly-5A1N]); and an encapsulation layer (SU-8 photoresist) on a flexible polyimide (PI) substrate (Fig. 1). Under a sufficient gate bias (V_g), NO molecules are oxidized to NO (nitrosonium ion) on the gate electrode and subsequently, converted to NO_2^- in the presence of OH^- (38):

$$NO - e^- \rightarrow NO^+ \quad [1]$$

$$NO + OH^- \rightarrow HNO_2. \quad [2]$$

The oxidation of NO on the gate electrode contributes to an increase in the potential at the electrolyte/channel interface, which pumps extra cations (M^+) from the electrolyte into the channel, compensating for the sulfonate anions of PSS (PSS^-) due to the formation of ionic bonds (M^+:PSS^-) (28). Consequently, holes (h^+) on PEDOT backbones are no longer coulombically stable, and $PEDOT^+$ is, therefore, converted from its conducting state to its insulating neutral state ($PEDOT^0$). The dedoping process results in a decrease in the drain current (I_{ds}) (39). The PEDOT:PSS channel can, therefore, transduce a small change in gate voltage signals into a large variation in drain currents, realizing the amplification of electrochemical signals, and the modulation process is described by a transfer curve. As the magnitude of the modulation increases with increasing NO levels, a correlation can be established between the drain current and NO concentration for real-time NO monitoring. Moreover, noble metals and carbon materials are common electrode materials for NO sensing. Noble metal electrodes, such as gold (Au) and platinum (Pt), show electroactivity toward NO to a certain extent. Carbon-based electrodes (e.g., carbon fiber or graphene) demonstrate the advantages of wider anodic potential windows and ease of chemical modification but require greater overpotentials for NO oxidation than noble electrodes (40). As Au electrodes are electrochemically and mechanically stable and have been successfully applied for NO sensing (17, 41), Au thin films are adopted as electrodes in the current work.

The fabrication process of NO sensors based on PEDOT:PSS is shown in *SI Appendix*, Fig. 1. Au thin-film electrodes (chromium [Cr]/Au, 5/100 nm) as the source, drain, and gate are patterned on a flexible PI substrate by photolithography. As silver/silver chloride (Ag/AgCl) is often adopted as an alternative gate material with a higher transconductance in OECTs (42, 43), external Ag/AgCl gate electrodes are also investigated for comparison, and the results will be discussed later. PEDOT:PSS serves as the active channel and is prepared via spin coating and patterning by photolithography and reactive oxygen etching (RIE).

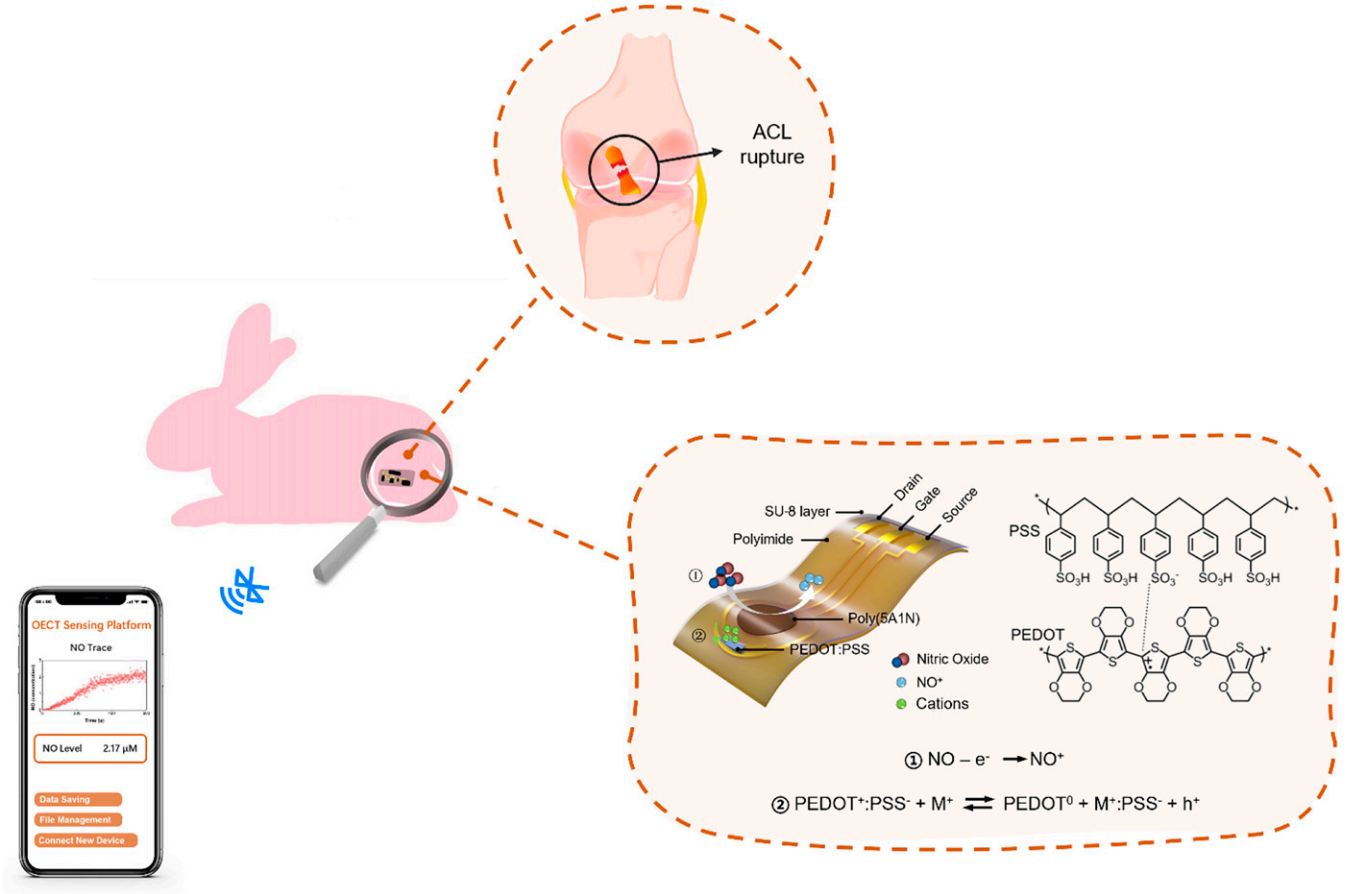

Fig. 1. Schematic illustration of the wireless NO sensing platform. The NO sensor comprises a PEDOT:PSS channel; Au thin films as the source, drain, and gate electrodes; poly-5A1N as the selective membrane on the gate; and SU-8 encapsulation only exposing the regions of the channel, poly-5A1N coated gate, and electrical contacts on a PI substrate. The electrochemical reaction of NO on the gate electrode modulates the doping state in the PEDOT:PSS channel. A correlation between the NO concentration and the channel current can, therefore, be established for NO sensing. The NO sensor is implanted in the articular cavity of a New Zealand White rabbit with ACL rupture for real-time monitoring of NO. The data are transmitted to a mobile phone through a customized wireless module through Bluetooth.

An insulating layer (SU-8 photoresist, 5 μm) is subsequently coated as an encapsulation, exposing only the area of PEDOT:PSS, poly-5A1N coated gate, and electrical contacts. To improve the selectivity of the NO sensor, gate electrodes are modified with poly-5A1N, which has demonstrated excellent selectivity for NO detection due to the increased permeability toward NO molecules and electrocatalytic effects facilitating electron transfer at the electrode surface (38, 44, 45). The thin poly-5A1N layer is realized by electropolymerization in 5-amino-1-naphthol (5A1N) solution (5 mM, pH 1) as reported previously (44) (*SI Appendix*, Fig. 2*A*). The initial cyclic voltammogram collected upon the electropolymerization of poly-5A1N (*SI Appendix*, Fig. 2*B*) and the Fourier transform infrared spectrometry (FTIR) results of the gate electrode before and after electropolymerization (*SI Appendix*, Fig. 2*C*) confirm that poly-5A1N is successfully achieved, with a thickness of ~22 nm (*SI Appendix*, Fig. 2*D*). An image of a fabricated NO device is shown in Fig. 2*A*.

Optimization of Channel Geometry and Gate Materials for NO Sensing. As PEDOT:PSS-based OECTs function in depletion mode, high gate voltages beyond the operational range will lead to the off state corresponding to a low transconductance ($g_m=\Delta I_{ds}/\Delta V_g$), which significantly impairs the amplification efficiency of OECTs. To enable robust NO sensing with PEDOT:PSS, achieving an appropriate transconductance under a high gate bias ($V_g \geq 0.8$ V) required for the oxidation of NO is, therefore, critical and has not been explored with reported PEDOT devices that often operate under a relatively low gate bias (<0.6 V). Since the transconductance of PEDOT:PSS channels has been shown to exhibit a strong dependence on the aspect ratio (*W/L*) of the channel (39, 46) and gate materials (37), the effects of channel geometry and different gate electrodes (Au and Ag/AgCl) have been studied. Multiple OECTs with aspect ratios (*W/L*) ranging from 10 to 1,000 have been fabricated to study the operational characteristics, as illustrated in Fig. 2*B* and *SI Appendix*, Fig. 3. As channels of different volumes yield different base currents, normalized transfer curves with respect to the channel current without applying the gate bias I_{ds}^0 are used to identify the desirable geometrical structure of the channels and gate materials. Representative normalized transfer curves and the corresponding calculated transconductance with Ag/AgCl as the gate electrode are given in Fig. 2 *C* and *D* and *SI Appendix*, Fig. 4 *A* and *B*. The results demonstrate a typical transfer curve of PEDOT:PSS working in depletion mode in the sense that a positive gate bias causes the dedoping of the channel and therefore, reduces the drain current until it reaches the off state (Fig. 2*C* and *SI Appendix*, Fig. 4*A*). With increasing *W/L* ratios, the gate voltage that reaches the maximum values of transconductance [$V_g(g_{m,max})$] increases (Fig. 2*D*). The maximum value of $g_m \approx 5.5$ mS is achieved at $V_g = 0.5$ V with the largest investigated *W/L* ratio of 1,000, and the device will reach the off state if a higher gate bias is

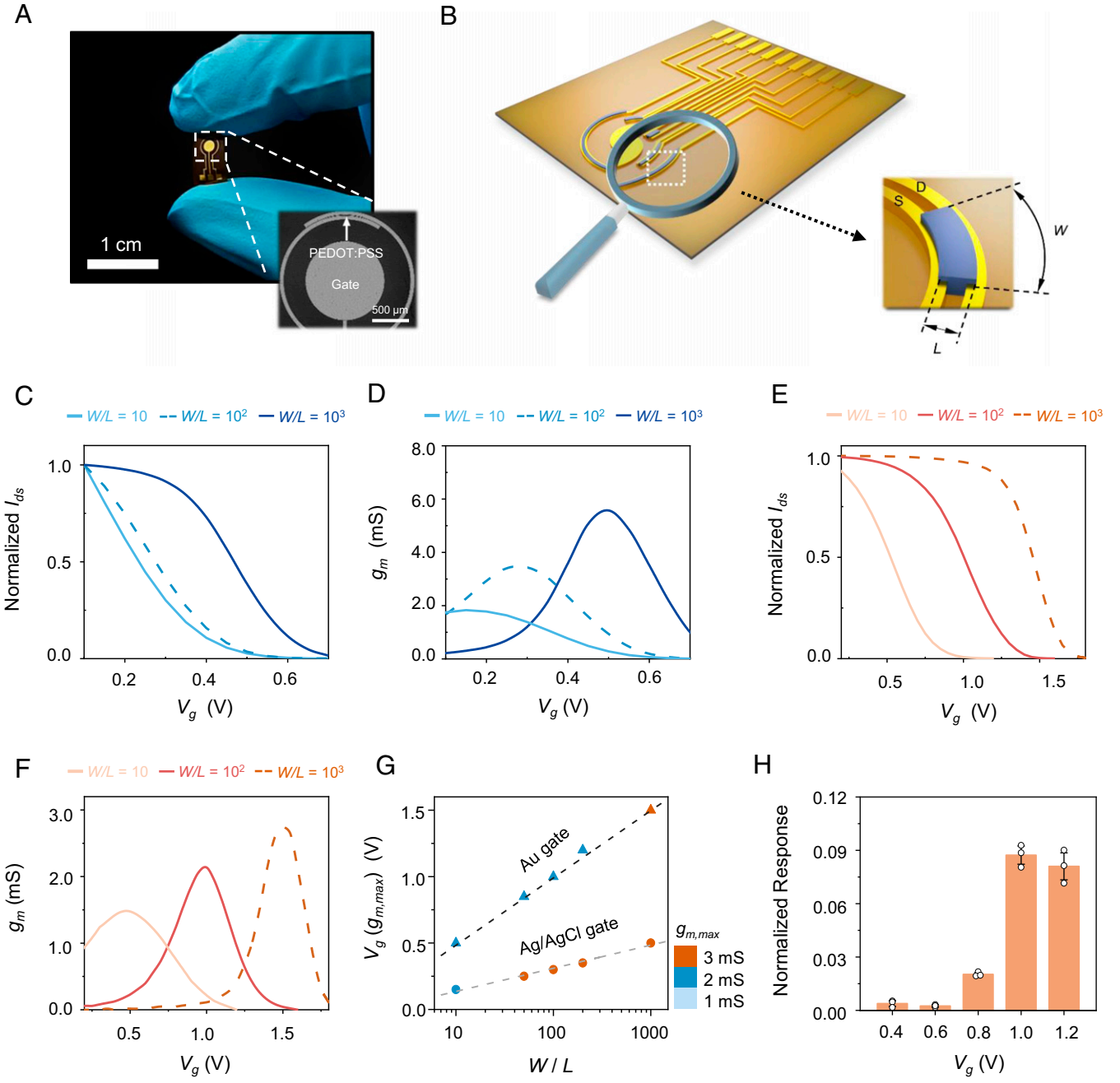

Fig. 2. Optimization of channel geometry and gate materials to achieve maximum transconductance at high gate biases desirable for NO sensing. (*A*) Photograph of a fabricated NO sensor based on OECTs. (*A*, *Inset*) The enlarged image of the PEDOT:PSS channel and Au electrodes. (*B*) Schematic illustration of multichannel PEDOT:PSS devices with different channel geometry. D, drain; *L*, length; S, source; *W*, width. (*B*, *Inset*) The enlarged illustration of the PEDOT:PSS channel. (*C* and *D*) Representative normalized transfer curves and transconductance of OECTs with Ag/AgCl gate electrodes, respectively (*W*/*L* ratios of 10, 10^2, and 10^3). (*E* and *F*) Representative normalized transfer curves and transconductance of OECTs with Au gate electrodes, respectively (*W*/*L* ratios of 10, 10^2, and 10^3). (*G*) V_g of maximum transconductance as a function of *W*/*L* for different gate electrodes. Values are color coded based on the maximum transconductance value. (*H*) NR of the channel current with the additions of NO (1 μM) under different gate biases (V_g).

applied (>0.6 V) (Fig. 2*D*). In contrast, the normalized transfer curves and transconductance of OECTs with Au as the gate electrode are given in Fig. 2 *E* and *F* and *SI Appendix*, Fig. 4 *C* and *D*. The results suggest a trend similar to that with the Ag/AgCl gate electrode, but the maximum transconductance can be achieved at even higher gate voltages due to the polarization nature of Au electrodes that contributes to the drop of potential at the gate surface where the chemical reaction occurs (26).

The relationships of the gate biases that achieve the maximum transconductance $V_g(g_{m,max})$ and the channel geometry (*W*/*L*) for different gate materials are summarized in Fig. 2*G*. The results indicate that by tuning the aspect ratio of PEDOT:PSS channels, desirable amplification capability can be achieved at a high gate bias with an Au electrode, allowing for the detection of NO with high oxidation potentials of ∼0.92 V (vs. Ag/AgCl) in phosphate-buffered saline (PBS) (*SI Appendix*, Fig. 5). OECTs with a *W*/*L* value of 100 and Au gate electrodes are, therefore, chosen to yield a $V_g(g_{m,max})$ of 1.0 V, which matches the requirement of NO sensing. The microscopic image of a PEDOT:PSS channel (*W*/*L* ratio of 100, 10 × 1,000 μm) is given in *SI Appendix*, Fig. 6, illustrating the miniaturized active region compared with the previously reported

flexible electrochemical NO sensor (17). Moreover, the transfer characteristics of PEDOT:PSS channels with the selected geometry remain unchanged under different bending statuses, suggesting desirable flexibility (*SI Appendix*, Fig. 7).

With the optimized channel geometry, the normalized responses (NRs) of the channel current with the addition of NO (1 μM) at different V_g values are investigated to verify the proper V_g for the measurement of NO, and the results appear in Fig. 2*H*. Specifically, the NRs of OECTs corresponding to a certain concentration of NO are calculated by the following equation (28):

$$NR = \left| \left(I_{ds}^{conc} - I_{ds}^{conc=0} \right) / I_{ds}^{conc=0} \right|, \quad [3]$$

where $I_{ds}^{conc=0}$ is the channel current without the addition of NO and I_{ds}^{conc} is the channel current with the addition of a certain concentration of NO. The highest NR is achieved with a gate voltage of 1.0 V, which further confirms the better performance of OECTs operated under $V_g(g_{m,max})$. The gate bias of 1.0 V is, therefore, selected for NO detection.

The leakage gate current across the source electrode (I_{gs}) is also investigated, and the results appear in *SI Appendix*, Fig. 8. The highest I_{gs} is lower than 0.17 μA, which is much smaller than the lowest drain current (1.65 μA) upon testing the transfer characteristics of NO devices with a gate bias swept up to 1.6 V and a drain voltage of −0.2 V (*SI Appendix*, Fig. 8*A*). The long-term gate leakage current is also maintained at a low level (∼50 nA) with a gate bias of 1.0 V and a drain voltage of −0.2 V (*SI Appendix*, Fig. 8*B*), indicating reliable sensing performance.

Device Characteristics of NO Sensors. A schematic diagram of the equivalent circuit and the associated potential difference between the gate and the channel of PEDOT:PSS devices are given in Fig. 3*A*. The equivalent circuit consists of two capacitors corresponding to the electrolyte/channel capacitance ($C_{E\text{-}C}$) and the gate/electrolyte capacitance ($C_{G\text{-}E}$) and a resistor corresponding to the electrolyte resistance (R_E). According to Bernard's model, the applied gate voltage drops at the gate/electrolyte interface and the electrolyte/channel interface assuming negligible potential changes in the electrolyte and within the channel. To achieve efficient gating to amplify electrochemical signals, $C_{G\text{-}E}/C_{E\text{-}C}$ greater than 10 is desirable as otherwise, a significant fraction of the applied gate voltage will drop at the gate/electrolyte interface (26). As the capacitance is closely

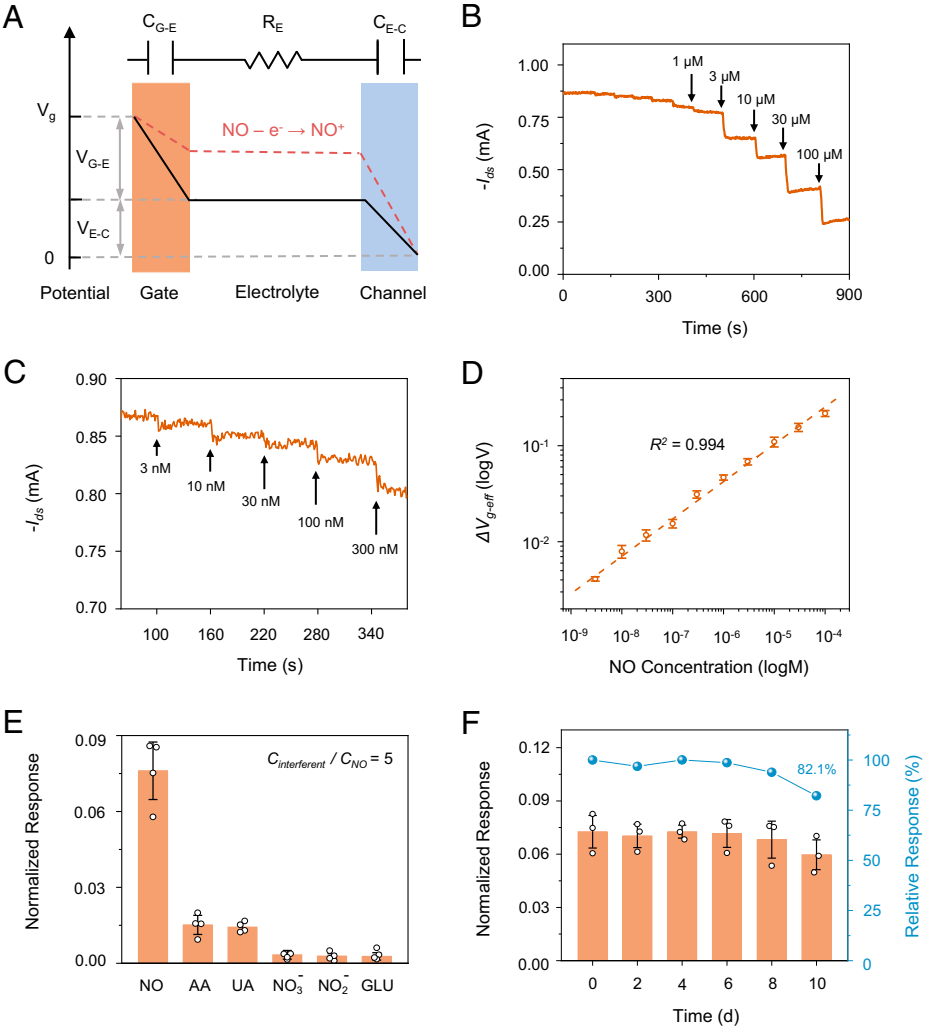

Fig. 3. Working principle and sensing performance of the NO sensor. (*A*) The equivalent circuit and potential diagram of the OECT-based NO sensor. Black solid lines indicate before NO oxidation; the red dashed line indicates after NO oxidation in PBS (pH 7.4). (*B* and *C*) Channel current responses as a function of NO concentrations from 3 nM to 100 mM (gate bias: 1.0 V; drain voltage: −0.2 V). (*D*) Calibration curve showing the relationship between the effective gate voltage changes $\Delta V_{g\text{-}eff}$ and NO concentrations in logarithmic scale. The dashed line indicates the linear fitting of the data. (*E*) Selectivity of the NO sensor: normalized current responses with the addition of NO (1 μM) and potentially interfering chemicals (5 μM). (*F*) Stability of the NO sensor: normalized current responses and relative current responses with respect to the initial channel current, with the addition of NO (1 mM) after storage in PBS for 0, 2, 4, 6, 8, and 10 d. In *D*–*F*, data are shown as the means ± SDs.

related to the size of the gate and the channel area, a larger gate electrode is, therefore, desirable for efficient gating. Specifically, both $C_{G\text{-}E}$ and $C_{E\text{-}C}$ of the NO sensor could be estimated. For example, $C_{G\text{-}E}$ of Au gate electrodes based on the electrical double layer is estimated to be ~447 nF (14.25 μF/cm^2, 3.14 × 0.1 × 0.1 cm^2) (47). $C_{E\text{-}C}$ at the electrolyte/PEDOT:PSS interface is estimated to be 31.2 nF (39 F/cm^3, 0.08 × 10 × 1,000 μm^3) (29). With current geometry, $C_{G\text{-}E}/C_{E\text{-}C}$ greater than 10 is achieved to assure efficient gating to amplify NO signals.

The oxidation of NO at the gate electrode increases the potential at the electrolyte/channel interface ($V_{E\text{-}C}$) while decreasing the potential at the gate/electrolyte interface ($V_{G\text{-}E}$). The change in $V_{G\text{-}E}$ will modulate the effective gate voltage test ($V_{g\text{-}eff}$) applied to the OECT device, which is related to the concentration of NO. The change in the effective gate voltage ($\Delta V_{g\text{-}eff}$) here can be described by (31)

$$\Delta V_{g-eff} \approx 2.30\ (1+\gamma)\ \frac{\kappa T}{2q}\ \log[analyte] + C, \qquad [4]$$

where γ is the ratio between $C_{E\text{-}C}$ and $C_{G\text{-}E}$ (Fig. 3*A*), κ is the Boltzmann constant, T is the absolute temperature, q is the charge of an electron, [*analyte*] is the concentration of NO in the biological solution, and C is a constant. For analytes with low concentrations, Eq. **2** can be simplified by the empirical relationship below (48):

$$\Delta V_{g-eff} \approx A \times [analyte]^{\beta}, \qquad [5]$$

where A and β are constants determined by the regression of experimental data, and a linear relationship can, therefore, be established between $\log(\Delta V_{g\text{-}eff})$ and the logarithmic concentration of NO to achieve a calibration curve.

Fig. 3 *B* and *C* shows the current response (I_{ds}) as a function of NO concentration in PBS, with a constant source–drain voltage (V_d = −0.2 V) and gate voltage (V_g = 1.0 V). The measured I_{ds} decreases in a step-like manner in accordance with increasing NO concentrations. The device achieves a response limit of 3 nM for NO detection and delivers significant current responses to NO concentrations ranging from 3 nM to 100 μM in PBS solutions. For quantitative analysis, the recorded I_{ds} is converted to the change in the effective gate voltage using the normalized transfer curve (*SI Appendix*, Fig. 9). The logarithmic change in the effective gate voltage $\log(\Delta V_{g\text{-}eff})$ vs. the logarithmic NO concentration follows a linear relationship ($R\Delta V_{g-eff}{}^2$ = 0.994), which matches Eq. **3** (Fig. 3*D*). The results demonstrate an excellent sensitivity of 94 mV/dec (corresponding to an averaged sensitivity of 174 μA/μM or 789 μS/μM in the concentration range of 0 to 1 μM) compared with previously reported NO sensors (*SI Appendix*, Table 1), attributed to the volumetric gating of the PEDOT channel, which yields a better amplification efficacy. Overall, these operational characteristics suggest that with optimized channel geometry and gate electrodes, PEDOT:PSS devices can function as high-performance sensors for NO detection.

The selectivity of NO sensors is investigated by involving interfering substances that are often present in biological systems, including GLU, sodium nitrite (nitrite), sodium nitrate (nitrate), AA, and UA. Although the concentrations of these chemicals vary significantly depending on biological environments, the physiological range of nitrite, GLU, AA, and UA has been estimated to be mostly in the range from nanomolar to micromolar (e.g., 0.1 to 2 μM for nitrite and 3 to 6 μM for GLU in saliva) (49–51). Considering the typical levels of potential interferences, chemicals (GLU, nitrite, nitrate, AA, UA) with a concentration of 5 μM are used in the selectivity evaluation. As L-arginine (L-Arg; 5 mM) and N$^{\omega}$-nitro-L-arginine methyl ester (L-NAME; 10 mM) are adopted to stimulate and inhibit NO generation, the associated current responses are also investigated to preclude potential interference with NO sensing. With the introduction of these interfering chemicals, no obvious current response is observed (Fig. 3*E* and *SI Appendix*, Fig. 10). In contrast, a significant change in drain current is captured with the addition of NO (1 μM). The results of the antiinterference performance of the NO sensor are summarized in Fig. 3*E*, demonstrating desirable selectivity over common interfering chemicals compared with the bare gate electrode without the modification of poly-5A1N (*SI Appendix*, Fig. 11). The excellent selectivity introduced by the poly-5A1N selective membrane is attributed to a better permeability toward NO over large interfering molecules (e.g., AA and UA) on the basis of size exclusion (52, 53). Moreover, poly-5A1N films can facilitate electron transfer to the electrode surface and enhance the NO response, which is also beneficial to selectivity improvement (44). In addition, the stability of the NO sensors is evaluated over a 10-d period. The normalized transfer curve remains almost unaffected after storage in PBS solution for 10 d (*SI Appendix*, Fig. 12*A*), and the sensors also show stable sensing performance for NO detection (*SI Appendix*, Fig. 12*B*). Moreover, the device retains 82.1% of the initial current response after 10 d (Fig. 3*F*), indicating an excellent operational time frame over a 10-d period.

Mouse fibroblasts (L929 cells) are cultured with NO sensors to evaluate biocompatibility. The combined fluorescent images with Calcein-AM/propidium iodide staining of cell growth after 5 d (Fig. 4*A*) show no significant difference between the NO sensor and control groups, indicating minimal cytotoxicity of the constituent materials.

Real-Time Monitoring of NO In Vitro. In vitro tests evaluating the sensing performance are carried out for real-time detection of NO produced in chondrocytes, where NOS converts L-Arg into NO and interleukin-1β (IL-1β) and L-NAME can function as NOS stimulators and inhibitors, respectively. Chondrocytes are cultured with the inflammatory cytokine IL-1β (10 ng mL^{-1}) in PBS at 37 °C to simulate the condition of OA (17, 54, 55). As illustrated in Fig. 4*B*, (A) L-Arg only, after L-Arg (5 mM) is introduced (at t = 2 h; group A), the drain current of the NO sensor drops significantly and continues to decrease progressively for ~5 h, followed by a gradual recovery to the initial state. In contrast, a negligible change in the drain current is observed either in chondrocytes treated with L-NAME (10 mM) and L-Arg (5 mM; group B) or in chondrocytes not treated with L-Arg or L-NAME (group C) (Fig. 4, [B] L-Arg + L-NAME and [C] control). The corresponding changes in NO concentrations appear in Fig. 4*C*, which is converted based on the calibration curve of the NO device in PBS shown earlier (Fig. 3*D*). The conversion method is elaborated in the methodology section. In comparison, a standard Griess test is performed in chondrocytes cultured with IL-1β and the addition of L-Arg (5 mM) to assess the amount of generated NO by sampling the solutions at different intervals (every 1 h) and measuring the associated nitrite (NO_2^-) concentration afterward (*SI Appendix*, Fig. 13). The results suggest a trend similar to that captured by the NO sensor (Fig. 4*B*, [A] L-Arg only) in the sense that the Griess test records the accumulated amount of NO, while the NO sensor is capable of continuous monitoring. Moreover, the calibration curve of the NO device after 10 h of continuous NO measurement remains almost unchanged (*SI Appendix*, Fig. 14), indicating desirable stability. These combined results demonstrate that the PEDOT:PSS-based sensors successfully

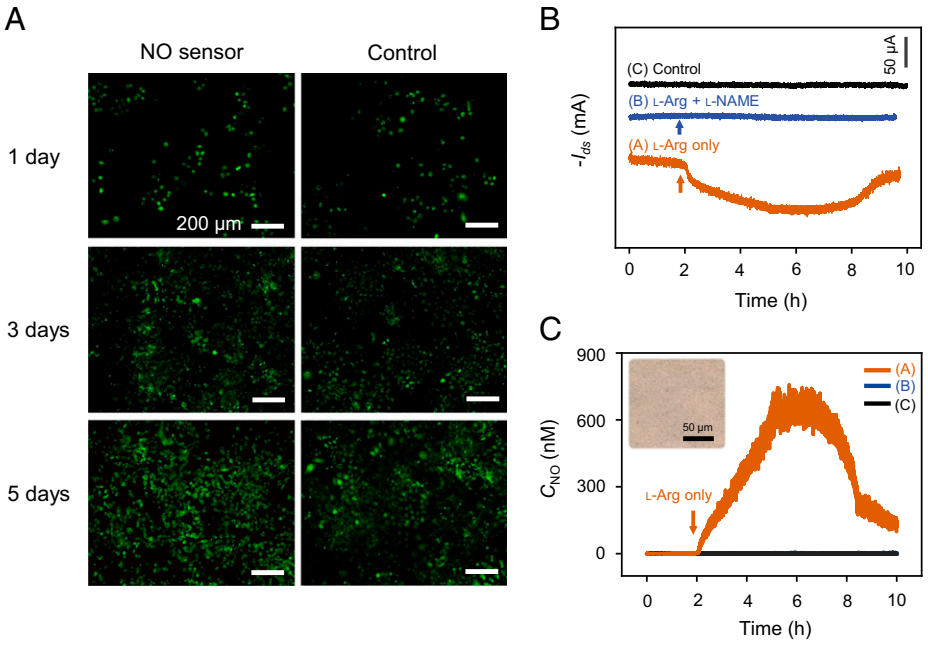

Fig. 4. Cell cytotoxicity evaluation of NO sensors with fibroblasts and the real-time monitoring of NO production in chondrocytes cultured with IL-1β at 37 °C. (*A*) Fluorescent images of fibroblast cells cultured on NO sensors for 1, 3, and 5 d with Calcein-AM/propidium iodide. Green (Calcein-AM) indicates live cells, and red (propidium iodide) indicates dead cells. (*B*) Real-time measurement of the drain current of the NO sensor over a 10-h period in chondrocytes. (*C*) Corresponding real-time NO concentrations in chondrocytes. (*C*, *Inset*) The optical microscope image of chondrocytes. In *B* and *C*, (A) L-Arg (5 mM) is added at $t = 2$ h to promote NO release, (B) L-NAME (10 mM) and L-Arg (5 mM) are added together at $t = 2$ h to inhibit NO production, and (C) the control group is without the addition of L-Arg or L-NAME. $n = 3$ independent experiments.

accomplish real-time monitoring of NO over a 10-h period in complex biological systems.

Real-Time Monitoring of NO In Vivo. ACL damage is one of the most prevalent knee injuries (56), and it is believed to contribute to the early progression of OA. Since chondrocyte apoptosis after cartilage damage has been linked to the increased production of proinflammatory cytokines and NO, real-time NO detection after ACL in the joint cavity could offer an essential early diagnosis to evaluate the development of OA (13, 57). To enable wireless measurement, a remotely controlled and battery-powered circuit module integrated with a customized cell phone application available for iPhone Operation System (iOS) devices and a Bluetooth connection has been realized for the data transmission of the NO sensors (Movie S1). A schematic diagram of the wireless module can be found in Fig. 5*A*, and the circuit design and system architecture are depicted in *SI Appendix*, Fig. 15. NO sensors are implanted in both sides of the articular cavity of New Zealand White rabbits and percutaneously connected to the wireless circuit secured on the thighs of the rabbits with surgical tape (Fig. 5*A*). Before the implantation of the devices, ACL transection surgery is performed on one side of the hind legs (ACL rupture group), and the other side remains unoperated (control group) (Fig. 5*B*). A photograph of the implanted device is shown in Fig. 5*C*. The X-ray image (Fig. 5*D*) identifies the implantation sites of the devices. The representative normalized transfer curve and the derived transconductance of NO sensors captured in the joint cavity align well with those acquired in PBS (Fig. 5*E*), indicating the feasibility of utilizing the in vitro calibration curve established in PBS (31, 58). Continuous and wireless NO detection is achieved over 8 d with a 10-min period every day. The recorded normalized signals of I_{ds} at 0, 2, 4, 6, and 8 d are given in Fig. 5*F*, and Fig. 5*G* summarizes the corresponding NO concentrations converted based on the calibration curve obtained in PBS shown earlier (Fig. 3*D*). The NO concentrations of the ACL rupture group remain at high levels over the monitoring period compared with the NO concentrations in the control group, which demonstrates relatively low NO generation with a decreasing pattern. The unstable current that occurs in the control group could result from the surgery-induced inflammatory response, which is inevitable (59). Nevertheless, the inflammation is believed to be mild, as no significant inflammation or swelling is observed at the surgical site within the NO monitoring window in most cases, and the retrieved sensors are not covered by obvious scar tissues. In addition, although surgery-induced inflammation could be present on both sides of the hind legs (control and ACL rupture groups), the NO concentration is much greater in the ACL rupture group, which is believed to be attributed to ACL injury–induced inflammation. NO sensors are subsequently removed from the articular cavity after the NO monitoring window. Histopathological investigations of associated femoral condyles are performed after 4, 6, and 8 wk of the initial implantation surgeries to reveal the potential correlations of early-stage NO release and cartilage degeneration at the later stage. The hematoxylin–eosin (HE) staining images of the femoral condyles from both the ACL rupture and control groups after 4, 6, and 8 wk of surgeries are shown in Fig. 5 *H* and *I* and *SI Appendix*, Fig. 16. In the control group, no obvious cartilage injury is observed in any of the HE staining images, which indicates the absence of OA and excellent biocompatibility of the implanted NO sensors. In the ACL rupture group, the histomorphology remains comparable with that of the control group up to 4 wk (*SI Appendix*, Fig. 16). However, degenerative morphology with an irregular cartilage surface and disordered distribution of chondrocytes are observed at 6 wk after the operation, suggesting signs of cartilage degeneration (*SI Appendix*, Fig. 16). Severe lesions are present in the HE staining images at 8 wk in the ACL rupture group (Fig. 5*H*, region 1), in which fibrosis-like tissues are noted (Fig. 5*H*, region 1), and the

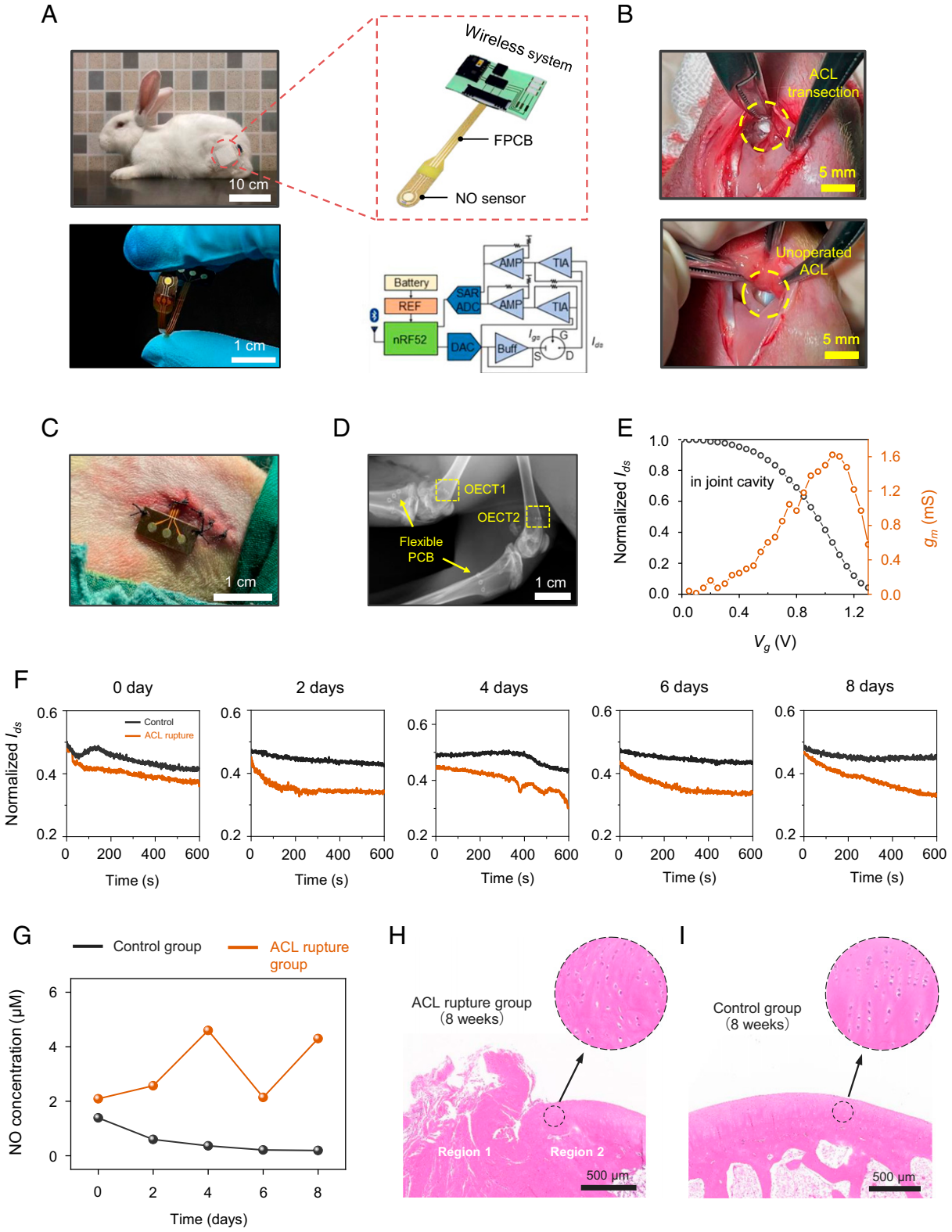

Fig. 5. Real-time monitoring of NO concentrations in the joint cavity of New Zealand rabbits. (A) Flexible high sensitivity NO sensing platform scheme. (*Top left*) Implant device is transdermally connected to a wireless module fixed to the thigh of a New Zealand rabbit. Schematic diagram of a NO sensor connected to a wireless module via FPCB (*top right*). (*Bottom left*) Photo of no sensor and FPCB. (*Bottom right*) wireless control and transmission system. REF, references; AMP, amplifiers; Buff, buffer; DAC, Digital-to-analog converters; SAR, successive approximation register analog-to-digital converter; TIA, transimpedance amplifier. (*B*) Photographs of transversely cut anterior cruciate ligament (*upper part*) and preoperative cruciate ligament (*lower part*). (*C*) A photograph of the implanted NO sensor in the joint cavity. (*D*) X-ray images of implanted NO sensors and FPCBs. Printed circuit boards, printed circuit boards. (*E*) Representative normalized transfer (black) and transconductance (red) curves of NO devices placed in the joint cavity of a Rabbit in New Zealand (gate voltages ranging from 0 to 1.3 V; Drain voltage: −0.2 V). (*F*) Real-time monitoring of normalized current response (*G*) in the joint cavity of New Zealand rabbits without and ACL rupture within 0, 2, 4, 6, 8 d above the concentration of no in the joint cavity. HE stained images of femoral condyle after 8 weeks of implantation in the (*H* and *I*) anterior cruciate rupture group and control group after surgery. (*H* and *I, Insets*) The enlarged view of HE staining images. In *F-I*, $n = 3$ independent experiments.

regular alignment of chondrocytes is lost compared with that in the healthy cartilage (Fig. 5*H*, region 2). The results indicate that early signs of high NO concentrations could be correlated with inflammation and cartilage degeneration at the later stage, which could potentially offer essential information to evaluate the progression to OA after ACL injury and optimize posttraumatic treatments.

Discuss

Advanced material and device strategies are proposed to enable a flexible and highly sensitive OECT-based biosensor for real-time NO monitoring in biological systems. The transconductance of the PEDOT:PSS channel is optimized by tuning the channel geometry and gate material to allow the desired amplification of the electrochemical signal for NO sensing. The high-performance NO sensors feature a wide sensing range (3 nM to 100 μM), low response limits (3 nM), high sensitivity (94 mV/dec), and ideal stability over 10 d (*SI Appendix*, Table 1). Compared to previously reported electrochemical NO sensors, referenceless sensors with miniaturized active sensing regions enable NO detection at a higher spatial resolution, allowing electrochemical signals to be mapped to provide comprehensive diagnostic information. Real-time monitoring of NO evolution in chondrocytes was achieved, with results comparable to those measured by standard Griyas tests. Rabbit in New Zealand in 8D time by integrating with custom circuit modules Continuous and wireless NO testing is done in the articular cavity, which can provide the necessary early diagnosis and preventive treatment for post-traumatic OA progression. Advances in device architecture can further miniaturize devices and enable device placement in a minimally invasive manner. The introduction of ultra-low modulus and stretchable sensor materials that mimic surrounding tissue, incorporated with anti-inflammatory drug coatings, can facilitate the mitigation of potential foreign body reactions due to device implantation. The integration and miniaturization of wireless modules with flexible materials enable conformal contact with skin surfaces and stable connections to implanted devices, minimizing the impact of potential motion on wireless NO recording. Based on similar device protocols, the wireless and real-time detection of other important biomarkers (e.g., various cytokines, neurotransmitters, etc.) with high sensitivity and spatial resolution can provide comprehensive information. Promising future directions also include integrating biosensors with microfluidic channels or stimulation systems capable of modulating chemical or electrical functions to enable closed-loop and multifunctional platforms. Overall, proposed material selection and equipment design can provide a critical engineering foundation for decoding health conditions at an early stage and maximizing the therapeutic effectiveness of associated degenerations and diseases.

Method

Manufacture of NO equipment based on OECT. Sensorless was manufactured on a flexible PI substrate (125 μm). Thin-film Au electrodes (5 nm Cr / 100 nm Au) are first deposited by magnetron sputtering and patterned by lithography and peeling processes. PEDOT: The PSS active layer is subsequently achieved by spin coating, lithography and RIE. Specifically, PEDOT:PSS (Clevios PH-1000; Xi'an Polymer Light Technology Co., Ltd.) first with 0.5mL ethylene glycol (AR; Beijing Lanyi Chemical Products Co., Ltd.), 10 μL dodecylbenzenesulfonate (90%; Shanghai Aladdin Biochemical Technology Co., Ltd.), and 0.1 ml of 3-glycidyloxypropyltrimethoxysilane (97%; J&K Scientific Ltd.) and stirred for 1 h to enhance conductivity and film stability. The PEDOT:PSS precursor dispersion is then spin-coated and annealed at 120 °C for 1 h, then patterned by lithography and RIE (90 mT pressure, 100 sccm O_2, 5 sccm SF_6, with 100 W for 120 seconds) enables channels (∼180 nm) with different *W/L* ratios (10, 50, 100, 200, 1,000). Channels with a *W/L* ratio of 10^2 (size: 10 × 1,000 μm) exhibits excellent sensitivity and was therefore chosen as the NO detection. A layer of SU-8 3005 photoresist (5 μm thick) is formed on the PI substrate as an encapsulation layer for the water electrolyte, exposing only the areas of the channel, source, drain and gate contacts. Finally, the gate electrode is functionalized using poly-5A1N to improve the detection specificity of NO. First clean the gate with acetone, isopropyl alcohol (IPA) and deionized water; 5 mM 5A1N (95%; Sigma-Aldrich) dissolves in PBS and uses HCl to titrate pH 1 (Modern Orientation Technology Development Co., Ltd.) to enhance solubility. Electropolymerization is performed on a clean gate electrode by cyclic voltammetry with a scanning speed of 50 mV s^{-1} from 0 to 0.8 V with 10 cycles. Pt and Ag/AgCl electrodes were employed as the counterelectrode and reference electrode, respectively. The gate electrode was then rinsed thoroughly in DI water to remove possible residues.

Preparation of Standard NO Solutions. Preparation of standard NO solutions was similar to that reported previously (17). Sulfuric acid solution (3 M) was added dropwise to a saturated nitrite sodium solution, resulting in the generation of NO gas, which was filtered twice through NaOH solutions (1 M). The saturated NO solution (1.9 mM, room temperature) was obtained by bubbling the produced NO gas into PBS solutions. To achieve a calibration curve of NO detection, the saturated solution was diluted with PBS to realize varied NO concentrations. Due to the reactive nature of NO, standard NO solutions were freshly made for each measurement.

Device Characterization. The electrical measurement of OECTs was performed on a Keithley 4200-SCS (Tektronix, Inc.) probe station. Considering that the ionic concentration of electrolyte could influence the performance of OECTs (26), we use PBS as the electrolyte to mimic the in vivo environment to evaluate the sensing performance of NO and obtain the calibration curve for the conversion of the data measured in vivo. Two gate materials were investigated, including the external Ag/AgCl wire electrode and the thin-film Au electrode, with PBS solutions as the electrolyte. To acquire transfer curves, V_d = –0.2 V was applied, with V_g sweeping from 0 to 1.6 V. Normalized transfer curves were obtained by normalizing the recorded drain current I_{ds} evoked by varied gate biases with respect to I_{ds}^0 (I_{ds} without applying the gate bias). For NO detection, devices were operated at $V_d = -0.2$ V and $V_g = 1.0$ V, and the transfer characteristics and the real-time drain current I_{ds} of NO sensors as a function of time were recorded. Based on the normalized transfer curve, recorded I_{ds} can be converted to , and a correlation can be established between the NO concentration and . The conversion procedure is as follows. 1) I_{ds} is first obtained before the addition of NO, which is defined as I_{ds}^{conc}. 2) After the addition of certain concentrations of NO, the corresponding I_{ds} value was obtained, which is defined as $I_{ds}^{conc=0}$. 3) The corresponding and can then be obtained using the transfer curve. 4) The absolute values of the difference between V_g^{conc} and $V_g^{conc=0}$ give $\Delta V_{g\text{-}eff}$. To obtain a uniform NO concentration for measurement in PBS, constant stirring was applied to achieve reliable calibration curves. For the selectivity investigation of NO sensors, drain currents I_{ds} with the addition of NO, GLU, sodium nitrite, sodium nitrate, AA, UA, L-Arg, and L-NAME are measured. The concentrations for NO and interference chemicals were 1 and 5 μM, respectively. L-Arg (5 mM) and L-NAME (10 mM) were also investigated as they could be potential interferences during the in vitro test. For the stability investigation, the sensor was immersed in PBS at 37 °C, and the transfer curves and calibration curves were obtained after 0, 5, and 10 d. The normalized current responses I_{ds} of the device to NO (1 μM) after 0, 2, 4, 6, 8, and 10 d of storage were also recorded.

Materials Characterization. Scanning electron microscopy images were obtained using an Auriga SEM/FIB Crossbeam System (ZEISS) at an electric voltage of 15 kV. FTIR measurements were obtained on a Nicolet 6700 (Thermo Fisher Scientific) in the range from 600 to 4,000 cm^{-1}. The optical microscopy images are taken by an optical microscope (MC-D800U; Phenix Optics Co., Ltd.).

Wireless Sensor Interface System. A wireless control and data transmission system was developed for the amplification, quantization, and scanning control of the NO sensing. The sensor interface features remote data communication to an iOS-based Graphic User Interface developed on a mobile phone through

Bluetooth. The wireless sensor interface consists of an analog front end, a digital control logic module, and a power management component using off-the-shelf components. Two transimpedance amplifiers, based on an optional amplifier, convert the collected gate–source current (I_{gs}) and drain–source current (I_{ds}) to voltages. An extra voltage amplifier was utilized for I_{ds} conversion. A control logic, regulating the analog front end with the digital to analog converter and the successive approximation register analog to digital converter, was implemented in a microprogrammed control unit (MCU), enabling the scanning of the voltage applied to the electrode. A customized iOS-based application dedicated to NO detection has been developed to realize wireless data transmission based on the Bluetooth module in the MCU. The software program realizes the binary decoding of Bluetooth and data plotting, which ensures the convenience of adjusting parameters and displaying real-time NO data. The software is compatible with iPhone and iPad for different application scenarios. The power management module includes Li battery charging and regulator circuits based on a low dropout regulator and reference for voltage. The entire power consumption of the circuit is less than 20 mW.

In Vitro Cytotoxicity Evaluation. According to the guidance of International Organization for Standardization (ISO) 10993-5: biological evaluation of medical devices–part 5: tests for in vitro cytotoxicity, Roswell Park Memorial Institute (RMPI)-1640 basal medium was used as the extraction media for the test. The electronic device was immersed in RMPI-1640 basal medium with the ratio of 3:1 between electronic device surface area (9.6 cm^2) and medium volume (3.2 mL) for 24 h at 37 °C. Subsequently, the extracts were filtered through the filter membrane (0.22 μm) before cells experiments. Meanwhile, L929 cells were seeded in 96-well plates at a density of 500 per well. After incubation for 24 h, the original medium was replaced by extracts (100% extracts) with 10% fetal bovine serum (FBS). Additionally, RPMI-1640 basal medium with 10% FBS was also used to incubate L929 cells as the control group. After 1, 3, and 5 d, Calcein-AM/propidium iodide (Biyuntian Co., Ltd.) staining was carried out, with green (Calcein-AM) for live cells and red (propidium iodide) for dead cells. The fluorescence images were obtained with fluorescence microscopy (Leica Microsystems Inc.).

In Vitro NO Measurement in Chondrocytes. Chondrocytes were obtained from the cartilage of Sprague-Dawley rats (7 d); details can be found in our previous work (17). Before the experiment, the cells were cultured in PBS (4 mL, 0.01 M) with IL-1β (100 μL, 10 ng mL^{-1}) with a cell density of $\sim 1 \times 10^6$ cells per well at 37 °C. For group (A), L-Arg (0.5 mL, 5 mM) was added to promote NO generation at $t = 2$ h. For group (B), L-Arg (0.5 mL, 5 mM) and L-NAME (0.5 mL, 10 mM) were added in sequence at $t = 2$ h, where L-NAME is added to inhibit NO generation. As a control experiment, no extra L-Arg or L-NAME was added in group (C). The corresponding changes of the drain current I_{ds} were recorded by the device. In addition, the standard Griess test was also performed to assess the amount of NO produced by the same batch of chondrocytes through sampling the solution every 1 h. Sampled solutions and the Griess reagent kit (Thermo Fisher Scientific) were coincubated for 30 min under room temperature. Finally, the absorbance at 562 nm of each sample was acquired by a spectrophotometer (Molecular Devices) to detect the concentration of NO_2^-.

Animal Surgery and In Vivo NO Detection. Animal procedures were performed in agreement with the institutional guidelines of the Beijing Institute of Traumatology and Orthopedics. Experimental protocols were reviewed and approved by the Institutional Animal Care and Use Committee at Beijing Institute of Traumatology and Orthopedics. Compounded ketamine was used as the anesthesia for the New Zealand White rabbits. A complete ACL rupture was performed on one side of the hind legs (ACL rupture group), while the ACL on the other side remained intact (control group; $n = 3$). NO sensors were implanted in both sides to wirelessly and continuously monitor NO levels for 8 d. Mupirocin ointment (GlaxoSmithKline PLC) was applied to the surgical sites for the first 3 d after surgeries to assist the healing of surgical incisions. Elizabethan collars were placed on rabbits to prevent the biting of flexible printed circuit board (FPCB) connectors. Continuous measurement of NO was performed under light aesthesia by the injection of compounded ketamine (Jiangsu Beikang Pharmaceutical Co., Ltd.) 5 min before NO measurement to minimize the influence of movements on wireless recordings. The variation of the channel current I_{ds} was recorded for 600 s every day, and the data were then converted to $\Delta V_{g\text{-}eff}$ using representative transfer curves measured in the joint cavity environment, which could be further converted to the values of NO concentration based on the calibration curve obtained in PBS. NO concentrations at the end of 600 s of each day were summarized for the ACL rupture and control groups for comparison. After the 8-d monitoring window, all the NO sensors were retrieved from the joint cavity through a surgical operation. Histological investigations of the femoral condyles of the rabbits were performed after 4, 6, and 8 wk of the initial implantation surgeries to reveal the pathological evolution of the joint cavity at the later stage of ACL injury. The femoral condyles were fixed in paraformaldehyde for 1 wk and decalcified for 6 wk. Then, they were subsequently embedded in paraffin wax, sliced into 4-μm-thick slices, and stained with HE. All the samples were examined under an optical microscope (MC-D800U; Phenix Optics Co., Ltd.).

Data, Materials, and Software Availability. All study data are included in the article and/or supporting information.

ACKNOWLEDGMENTS. This project was supported by National Natural Science Foundation of China Grants 51971116 (to L.Z.), 92164202 (to M. Zhang), 52171239 (to L.Y.), and T2122010 (to L.Y.); Tsinghua University–Peking Union Medical College Hospital Initiative Scientific Research Program Grant 20191080592; Beijing Municipal Health Commission Grant BMC2021-6; and UTokyo–Tsinghua Collaborative Research Fund Grant 20213080033.

Author affiliations: [a]School of Materials Science and Engineering, The Key Laboratory of Advanced Materials of Ministry of Education, State Key Laboratory of New Ceramics and Fine Processing, Center for Flexible Electronics Technology, Tsinghua University, Beijing 100084, China; [b]Laboratory of Musculoskeletal Regenerative Medicine, Beijing Institute of Traumatology and Orthopaedics, Beijing 100035, China; [c]Department of Electronic Engineering, Tsinghua University, Beijing 100084, China; [d]Department of Engineering Science and Mechanics, The Pennsylvania State University, University Park, PA 16802; [e]College of Engineering, Peking University, Beijing 100084, China; [f]State Key Laboratory of Powder Metallurgy, Powder Metallurgy Research Institute, Central South University, Changsha, Hunan 410083, China; [g]Animal Center, Beijing Institute of Traumatology and Orthopaedics, Beijing 100035, China; [h]Beijing Engineering Research Center of Mixed Reality and Advanced Display, School of Optics and Photonics, Beijing Institute of Technology, Beijing 100081, China; [i]Department of Electronic Engineering, Beijing National Research Center for Information Science and Technology, Institute for Precision Medicine, Center for Flexible Electronics Technology and IDG/McGovern Institute for Brain Research, Tsinghua University, Beijing 100084, China; and [j]Beijing Institute of Collaborative Innovation, Beijing Siweizhigan Co., Ltd., Beijing 100084, China

Author contributions: Y.D., H.Q., X.S., M. Zhang, and L.Y. designed research; Y.D., H.Q., Y.M., S.L., M. Zhao, Z.G., Y.J., R.Z., J.J., H.D., G.L., K.Z., R.L., H.C., and L.Z. performed research; Y.D., H.Q., Y.M., K.C., X.S., M. Zhang, and L.Y. analyzed data; and Y.D., H.Q., X.S., M. Zhang, and L.Y. wrote the paper.

1. U. Förstermann, W. C. Sessa, Nitric oxide synthases: Regulation and function. *Eur. Heart J.* **33**, 829–837 (2012).
2. V. Calabrese *et al.*, Nitric oxide in the central nervous system: Neuroprotection versus neurotoxicity. *Nat. Rev. Neurosci.* **8**, 766–775 (2007).
3. F. J. Blanco, R. L. Ochs, H. Schwarz, M. Lotz, Chondrocyte apoptosis induced by nitric oxide. *Am. J. Pathol.* **146**, 75–85 (1995).
4. D. E. Prince, J. K. Greisberg, Nitric oxide-associated chondrocyte apoptosis in trauma patients after high-energy lower extremity intra-articular fractures. *J. Orthop. Traumatol.* **16**, 335–341 (2015).
5. S. B. Abramson, Nitric oxide in inflammation and pain associated with osteoarthritis. *Arthritis Res. Ther.* **10** (suppl. 2), S2 (2008).
6. P. Jin *et al.*, Nitric oxide nanosensors for predicting the development of osteoarthritis in rat model. *ACS Appl. Mater. Interfaces* **9**, 25128–25137 (2017).
7. N. Singh, International epidemiology of anterior cruciate ligament injuries. *Orthopedic Research Online Journal* **1**, 94–96 (2018).
8. J. Aguilar, J. Yang, "Anterior cruciate ligament (ACL) injury: A literature review" in *Proceedings of the ASME 2017 International Design Engineering Technical Conferences and Computers and Information in Engineering Conference* (ASME, 2017, pp. 1–10).
9. N. A. Friel, C. R. Chu, The role of ACL injury in the development of posttraumatic knee osteoarthritis. *Clin. Sports Med.* **32**, 1–12 (2013).
10. E. J. Clarke, J. R. Anderson, M. J. Peffers, Nuclear magnetic resonance spectroscopy of biofluids for osteoarthritis. *Br. Med. Bull.* **137**, 28–41 (2021).
11. G. Sakellariou *et al.*, EULAR recommendations for the use of imaging in the clinical management of peripheral joint osteoarthritis. *Ann. Rheum. Dis.* **76**, 1484–1494 (2017).
12. S. Hashimoto *et al.*, Nitric oxide production and apoptosis in cells of the meniscus during experimental osteoarthritis. *Arthritis Rheum.* **42**, 2123–2131 (1999).
13. M. C. de Andrés, E. Maneiro, M. A. Martín, J. Arenas, F. J. Blanco, Nitric oxide compounds have different effects profiles on human articular chondrocyte metabolism. *Arthritis Res. Ther.* **15**, R115 (2013).

14. Y. Y. Woldman *et al.*, Detection of nitric oxide production in cell cultures by luciferin-luciferase chemiluminescence. *Biochem. Biophys. Res. Commun.* **465**, 232–238 (2015).
15. J. Ren *et al.*, A comparative ESR study on blood and tissue nitric oxide concentration during renal ischemia-reperfusion injury. *Appl. Magn. Reson.* **32**, 243–255 (2007).
16. H. Kojima *et al.*, Fluorescent indicators for imaging nitric oxide production. *Angew. Chem. Int. Ed. Engl.* **38**, 3209–3212 (1999).
17. R. Li *et al.*, A flexible and physically transient electrochemical sensor for real-time wireless nitric oxide monitoring. *Nat. Commun.* **11**, 3207 (2020).
18. I. R. Davies, X. Zhang, Nitric oxide selective electrodes. *Methods Enzymol.* **436**, 63–95 (2008).
19. G. Scheiblin, R. Coppard, R. M. Owens, P. Mailley, G. G. Malliaras, Referenceless pH sensor using organic electrochemical transistors. *Adv. Mater. Technol.* **2**, 11600141 (2017).
20. A. Libanori, G. Chen, X. Zhao, Y. Zhou, J. Chen, Smart textiles for personalized healthcare. *Nat. Electron.* **5**, 142–156 (2022).
21. A. Marks, S. Griggs, N. Gasparini, M. Moser, Organic electrochemical transistors: An emerging technology for biosensing. *Adv. Mater. Interfaces* **9**, 2102039 (2022).
22. S. Jiang *et al.*, Real-time electrical detection of nitric oxide in biological systems with sub-nanomolar sensitivity. *Nat. Commun.* **4**, 2225 (2013).
23. P. Leleux *et al.*, Organic electrochemical transistors for clinical applications. *Adv. Healthc. Mater.* **4**, 142–147 (2015).
24. J. Rivnay, R. I. M. Owens, G. G. Malliaras, The rise of organic bioelectronics. *Chem. Mater.* **26**, 679–685 (2014).
25. I. Gualandi *et al.*, Organic electrochemical transistors as versatile analytical potentiometric sensors. *Front. Bioeng. Biotechnol.* **7**, 354 (2019).
26. J. Rivnay *et al.*, Organic electrochemical transistors. *Nat. Rev. Mater.* **3**, 17086 (2018).
27. H. Tang, F. Yan, P. Lin, J. Xu, H. L. Chan, Highly sensitive glucose biosensors based on organic electrochemical transistors using platinum gate electrodes modified with enzyme and nanomaterials. *Adv. Funct. Mater.* **21**, 2264–2272 (2011).
28. D. A. Bernards *et al.*, Enzymatic sensing with organic electrochemical transistors. *J. Mater. Chem.* **18**, 116–120 (2008).
29. J. Rivnay *et al.*, High-performance transistors for bioelectronics through tuning of channel thickness. *Sci. Adv.* **1**, e1400251 (2015).
30. G. D. Spyropoulos, J. N. Gelinas, D. Khodagholy, Internal ion-gated organic electrochemical transistor: A building block for integrated bioelectronics. *Sci. Adv.* **5**, eaau7378 (2019).
31. K. Xie *et al.*, Organic electrochemical transistor arrays for real-time mapping of evoked neurotransmitter release in vivo. *eLife* **9**, e50345 (2020).
32. X. Xi *et al.*, Manipulating the sensitivity and selectivity of OECT-based biosensors via the surface engineering of carbon cloth gate electrodes. *Adv. Funct. Mater.* **30**, 1905361 (2020).
33. A. M. Pappa *et al.*, Organic transistor arrays integrated with finger-powered microfluidics for multianalyte saliva testing. *Adv. Healthc. Mater.* **5**, 2295–2302 (2016).
34. X. Ji *et al.*, Highly sensitive metabolite biosensor based on organic electrochemical transistor integrated with microfluidic channel and poly(N-vinyl-2-pyrrolidone)-capped platinum nanoparticles. *Adv. Mater. Technol.* **1**, 1600042 (2016).
35. M. Braendlein *et al.*, Lactate detection in tumor cell cultures using organic transistor circuits. *Adv. Mater.* **29**, 1605744 (2017).
36. H. Liu *et al.*, Ultrafast, sensitive, and portable detection of COVID-19 IgG using flexible organic electrochemical transistors. *Sci. Adv.* **7**, eabg8387 (2021).
37. P. R. Paudel, J. Tropp, V. Kaphle, J. D. Azoulay, B. Lüssem, Organic electrochemical transistors from device models to a targeted design of materials. *J. Mater. Chem. C Mater. Opt. Electron. Devices* **9**, 9761–9790 (2021).
38. T. Xu *et al.*, Electrochemical sensors for nitric oxide detection in biological applications. *Electroanalysis* **26**, 449–468 (2014).
39. J. T. Friedlein, R. R. McLeod, J. Rivnay, Device physics of organic electrochemical transistors. *Org. Electron.* **63**, 398–414 (2018).
40. M. D. Brown, M. H. Schoenfisch, Electrochemical nitric oxide sensors: Principles of design and characterization. *Chem. Rev.* **119**, 11551–11575 (2019).
41. N. Wenninger *et al.*, Development of an electrochemical sensor for nitric oxide based on carbon paste electrode modified with Nafion, gold nanoparticles and graphene nanoribbons. *Sens. Actuators B Chem.* **346**, 130532 (2021).
42. F. Lin, M. C. Lonergan, Gate electrode processes in an electrolyte-gated transistor: Non-Faradaically versus Faradaically coupled conductivity modulation of a polyacetylene ionomer. *Appl. Phys. Lett.* **88**, 133507 (2006).
43. G. Tarabella *et al.*, Effect of the gate electrode on the response of organic electrochemical transistors. *Appl. Phys. Lett.* **97**, 123304 (2010).
44. M. D. Brown, M. H. Schoenfisch, Nitric oxide permselectivity in electropolymerized films for sensing applications. *ACS Sens.* **1**, 1453–1461 (2016).
45. J. Ho Shim, H. Do, Y. Lee, Simple fabrication of amperometric nitric oxide microsensors based on electropolymerized membrane films. *Electroanalysis* **22**, 359–366 (2010).
46. J. Rivnay *et al.*, Organic electrochemical transistors with maximum transconductance at zero gate bias. *Adv. Mater.* **25**, 7010–7014 (2013).
47. S. E. Moulton, J. N. Barisci, A. Bath, R. Stella, G. G. Wallace, Studies of double layer capacitance and electron transfer at a gold electrode exposed to protein solutions. *Electrochim. Acta* **49**, 4223–4230 (2004).
48. M. Zhang *et al.*, High-performance dopamine sensors based on whole-graphene solution-gated transistors. *Adv. Funct. Mater.* **24**, 978–985 (2014).
49. M. Xu, D. Obodo, V. K. Yadavalli, The design, fabrication, and applications of flexible biosensing devices. *Biosens. Bioelectron.* **124-125**, 96–114 (2019).
50. N. S. Bryan *et al.*, Nitrite is a signaling molecule and regulator of gene expression in mammalian tissues. *Nat. Chem. Biol.* **1**, 290–297 (2005).
51. X. Deng *et al.*, Synthesis of merit-combined antimony tetroxide nanoflowers/reduced graphene oxide to synergistically boost real-time detection of nitric oxide released from living cells for high sensitivity. *J. Colloid Interface Sci.* **581** (part B), 465–474 (2021).
52. M. Badea *et al.*, New electrochemical sensors for detection of nitrites and nitrates. *J. Electroanal. Chem. (Lausanne)* **509**, 66–72 (2001).
53. J. H. Shim, Y. Lee, Amperometric nitric oxide microsensor based on nanopore-platinized platinum: The application for imaging NO concentrations. *Anal. Chem.* **81**, 8571–8576 (2009).
54. Y. Y. C. Lo, J. M. S. Wong, T. F. Cruz, Reactive oxygen species mediate cytokine activation of c-Jun NH2-terminal kinases. *J. Biol. Chem.* **271**, 15703–15707 (1996).
55. K. Sudo, Y. Takezawa, S. Kohsaka, K. Nakajima, Involvement of nitric oxide in the induction of interleukin-1 beta in microglia. *Brain Res.* **1625**, 121–134 (2015).
56. M. L. Killian, R. C. Haut, T. L. Haut Donahue, Acute cell viability and nitric oxide release in lateral menisci following closed-joint knee injury in a lapine model of post-traumatic osteoarthritis. *BMC Musculoskelet. Disord.* **15**, 297–297 (2014).
57. S. Hashimoto, K. Takahashi, D. Amiel, R. D. Coutts, M. Lotz, Chondrocyte apoptosis and nitric oxide production during experimentally induced osteoarthritis. *Arthritis Rheum.* **41**, 1266–1274 (1998).
58. W. Li, J. Jin, T. Xiong, P. Yu, L. Mao, Fast-scanning potential-gated organic electrochemical transistors for highly sensitive sensing of dopamine in living rat brain. *Angew. Chem. Int. Ed. Engl.* **61**, e202204134 (2022).
59. F. Paruk, J. M. Chausse, Monitoring the post surgery inflammatory host response. *J. Emerg. Crit. Care Med.* **3**, 47–60 (2019).

PNAS

Supplementary Information for

A flexible and highly sensitive organic electrochemical transistor-based biosensor for continuous and wireless nitric oxide detection

Yuping Deng, Hui Qi, Yuan Ma, Shangbin Liu, Mingyou Zhao, Zhenhu Guo, Yongsheng Jie, Rui Zheng, Jinzhu Jing, Kuntao Chen, He Ding, Guoqing Lv, Kaiyuan Zhang, Rongfeng Li, Huanyu Cheng, Linyun Zhao, Xing Sheng, Milin Zhang, Lan Yin

Lan Yin; Milin Zhang
Email: lanyin@tsinghua.edu.cn; zhangmilin@tsinghua.edu.cn

This PDF file includes:

Other supplementary materials for this manuscript include the following:

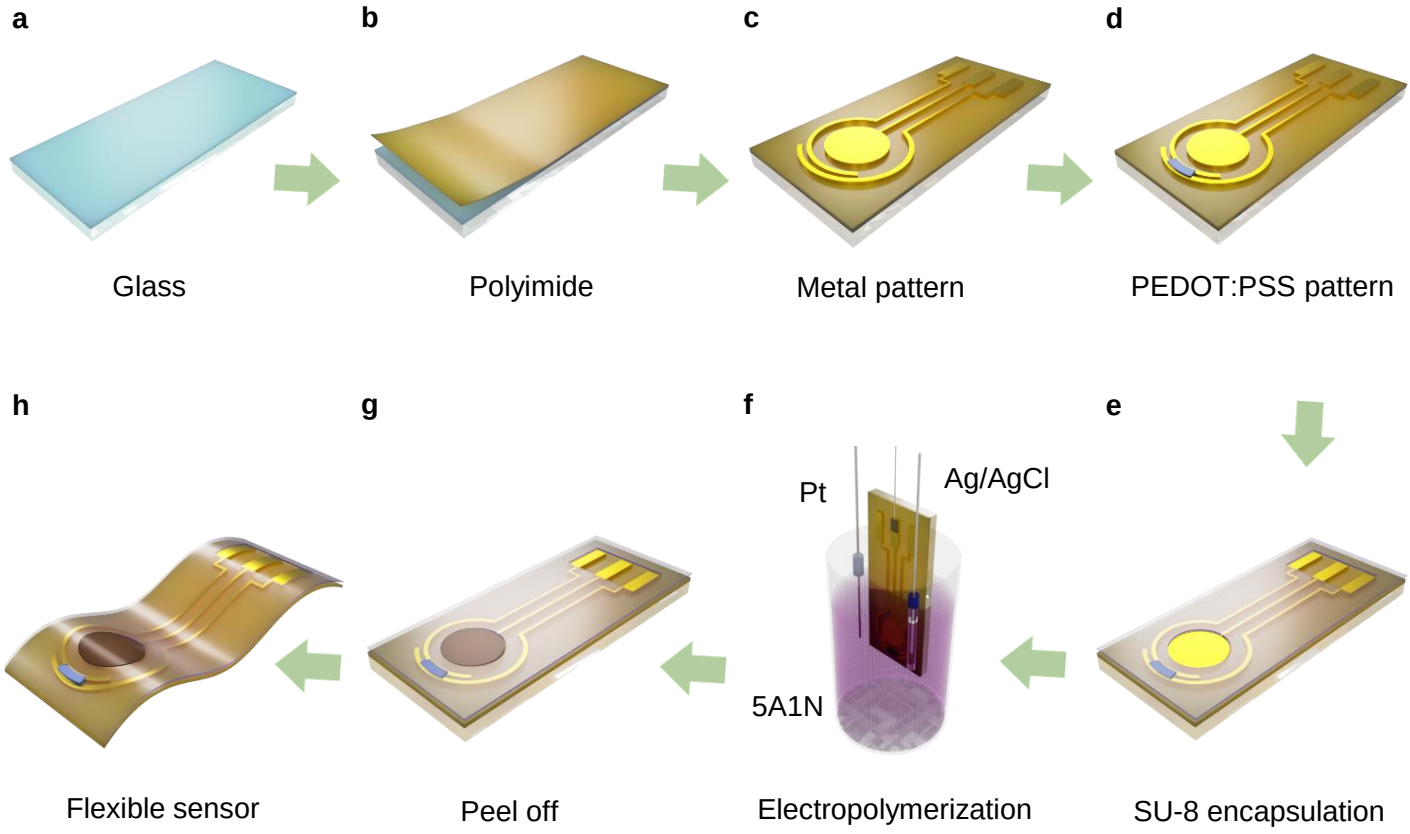

Supplementary Fig. 1: Fabrication process of the flexible NO sensor based on OECTs. a, PDMS spin-coating on a glass substrate. **b,** A PI substrate is laminated on the PDMS coating. **c,** Au electrodes are deposited by magnetron sputtering on the PI substrate. **d.** Patterning of the PEDOT:PSS channel between source and drain electrodes. **e,** A layer of SU-8 encapsulation is applied exposing the regions of gate, PEDOT:PSS channel, source, drain and gate contacts. **f,** Electropolymerization of a layer of poly-5A1N as the selective membrane on the gate electrode. **g, h,** The device is peeled off from the PDMS-coated glass to achieve a flexible NO sensor.

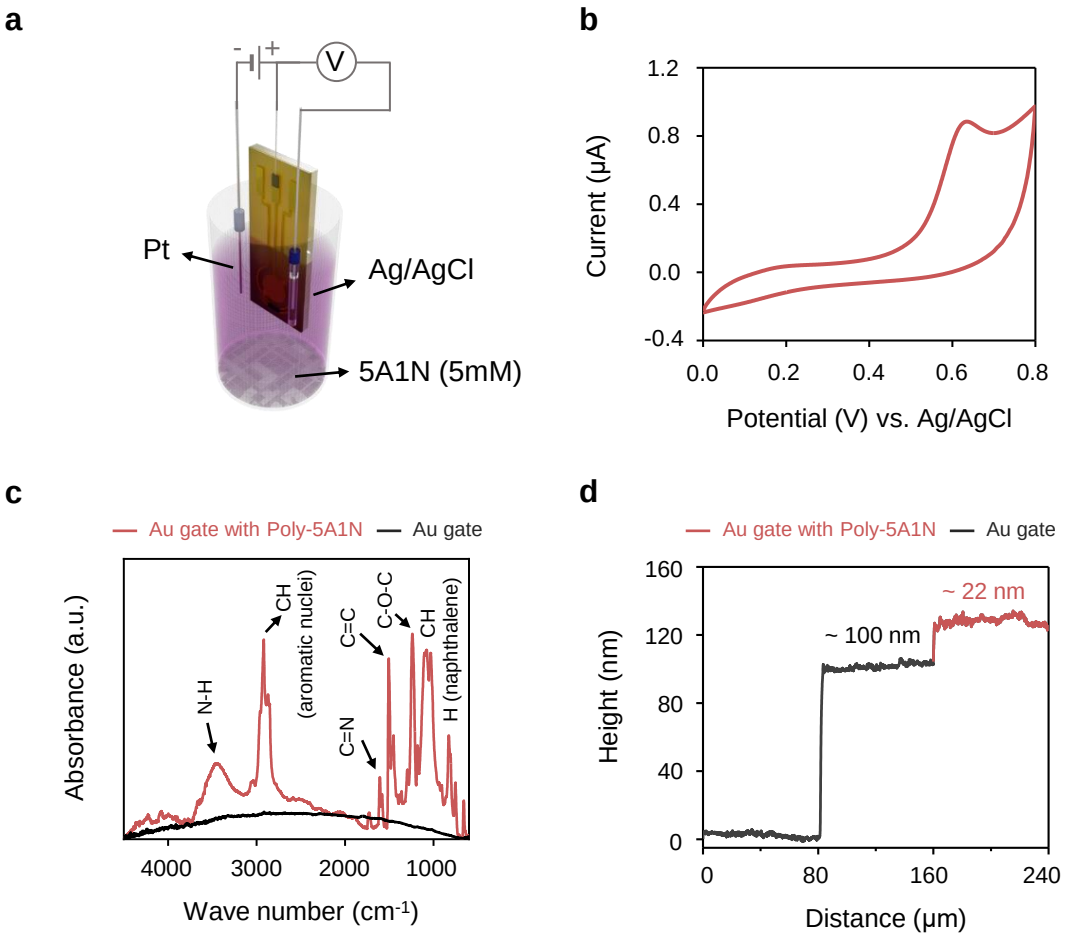

Supplementary Fig. 2: Electropolymerization of poly-5A1N on the gate electrode of the NO sensor. a, Schematic diagram of the experimental set-up for the electrodeposition of poly-5A1N. **b,** The first cycle of cyclic voltammetry of poly-5A1N electropolymerization with 5 mM 5A1N monomer solution. **c,** FTIR curves of the gate electrode of the NO sensor before and after electropolymerization. **d,** Height profile of the gate electrode of the NO sensor after electropolymerization of poly-5A1N.

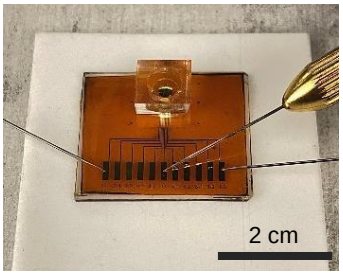

Supplementary Fig. 3: Photograph of a multi-channel PEDOT:PSS devices with different *W/L* ratios (10, 50, 100, 200, 1000) measured on a probe station in a PDMS well (2 mm in diameter, 3 mm in depth).

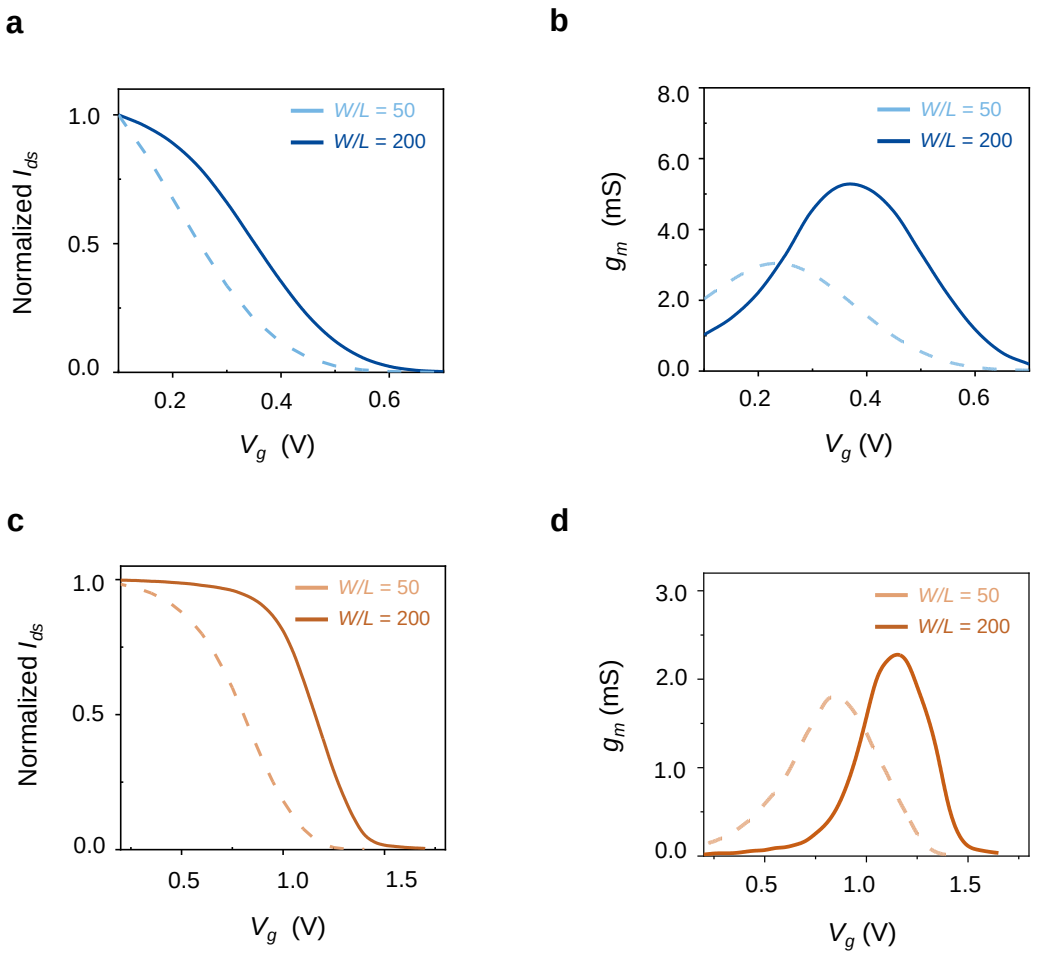

Supplementary Fig. 4: Optimization of channel geometry and gate materials to achieve maximum transconductance at high gate biases desirable for NO sensing (*W/L* ratio of 50 and 200). a, b, Representative normalized transfer curves and transconductance of OECTs with Ag/AgCl gate electrodes, respectively. **c, d,** Representative normalized transfer curves and transconductance of OECTs with Au gate electrodes, respectively.

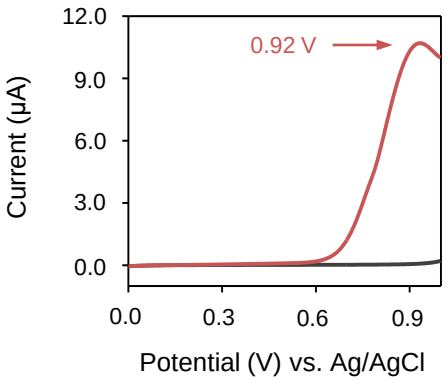

Supplementary Fig. 5: Linear sweep voltammetry (LSV) to identify the oxidation potential of NO, with the gate electrode of PEDOT device as the working electrode, Pt wire as the counting electrode and Ag/AgCl as the reference electrode. Current response is measured in blank (black) and PBS solutions with 1.9 mM NO (red). LSV scan rate: 50 mV s^{-1}.

a

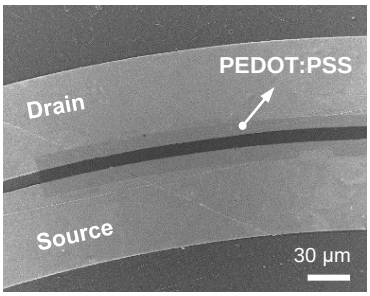

b

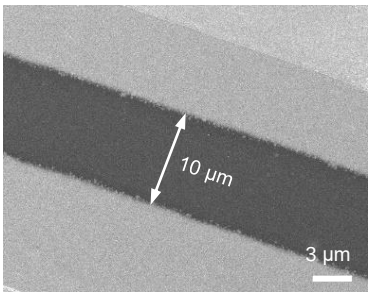

Supplementary Fig. 6: SEM images of PEDOT:PSS channels at different magnifications.

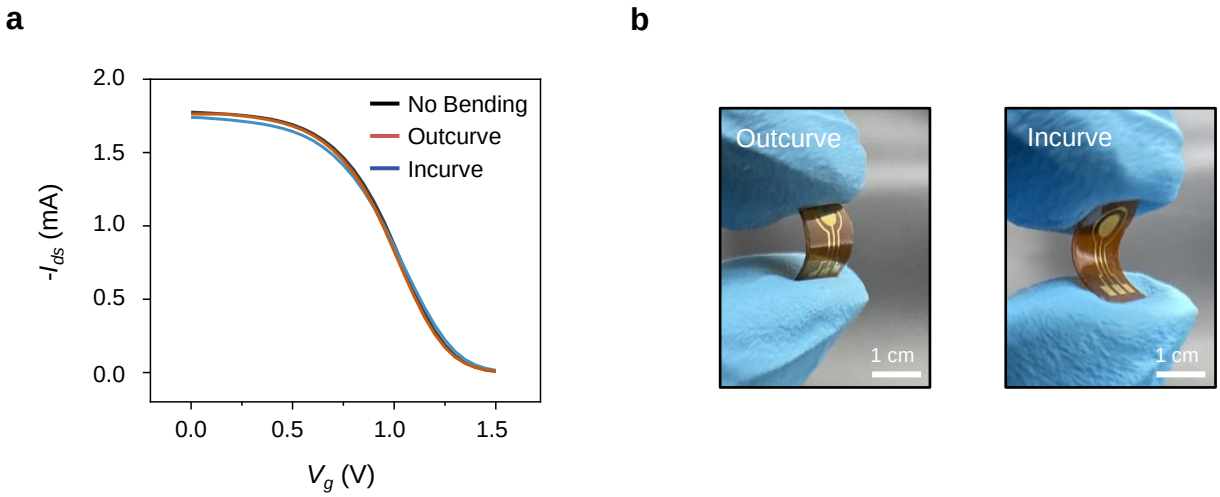

Supplementary Fig. 7: a, Transfer characteristics of the flexible PEDOT:PSS based OECT in PBS solutions with different bending status. **b,** Photographs of the flexible PEDOT:PSS based OECTs bent to both sides.

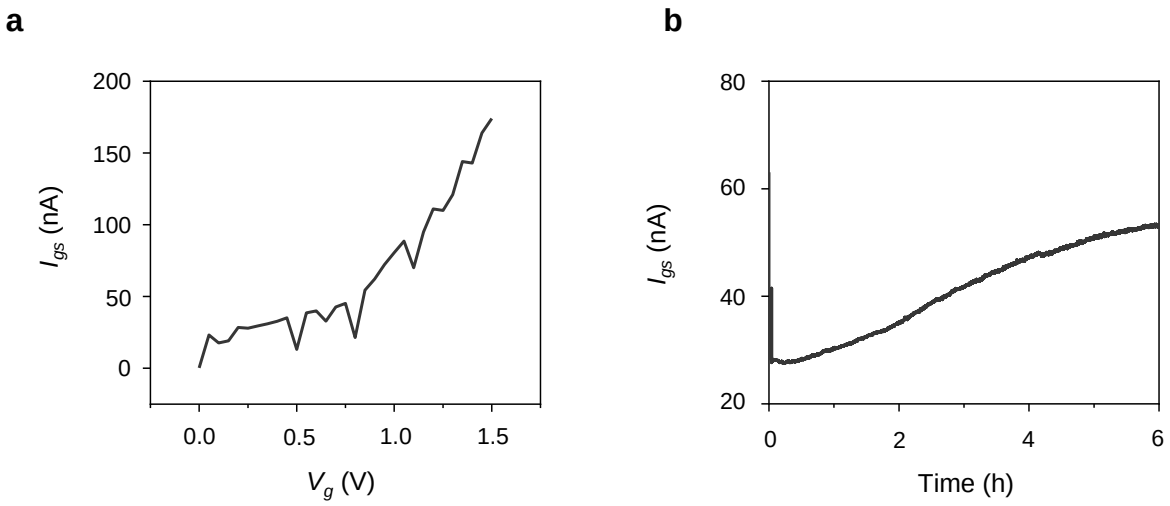

Supplementary Fig. 8: Gate leakage current (I_{gs}) of OECTs upon operation in PBS. a, Gate leakage current (I_{gs}) during the course of the recording of transfer characteristics. The gate bias is swept from 0 to 1.6 V with a step of 0.05 V and the drain voltage is fixed at -0.2 V. **b,** Long-term gate leakage current (gate bias: 1.0 V; drain voltage: -0.2 V).

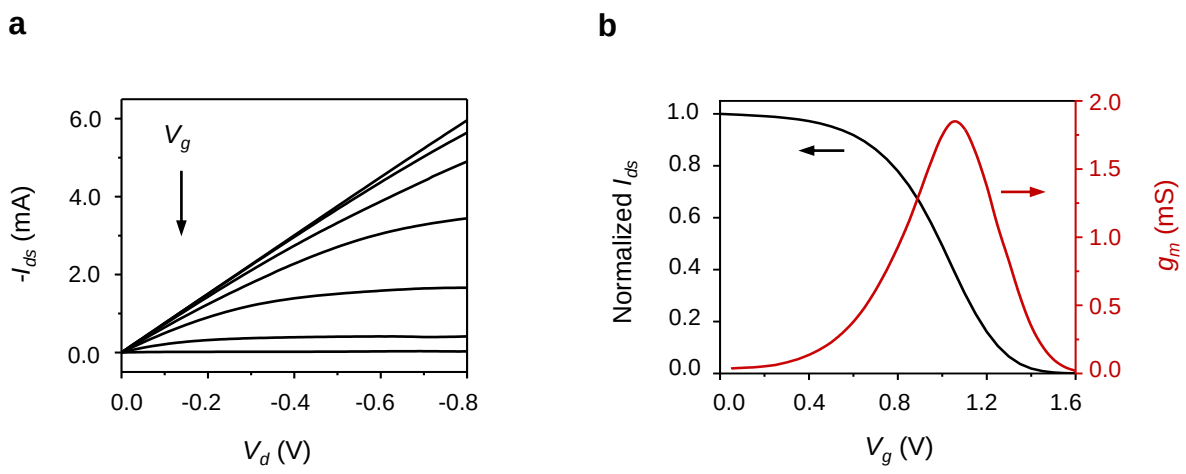

Supplementary Fig. 9: Device characteristics of the NO sensor in PBS with optimized channel geometry and gate materials. a, Drain current (I_{ds}) as a function of drain voltage (V_d) for gate voltages (V_g) varying from 0 (top curve) to +1.5 V (bottom curve) with a step of +0.25 V. **b,** Normalized transfer curve of the device. The channel dimensions are 10 µm in length and 1000 µm in width, with Au gate electrode coated with Poly-5A1N. The gate potentials are swept from 0 to 1.6 V with a step of 0.05 V while drain voltage is fixed at -0.2 V.

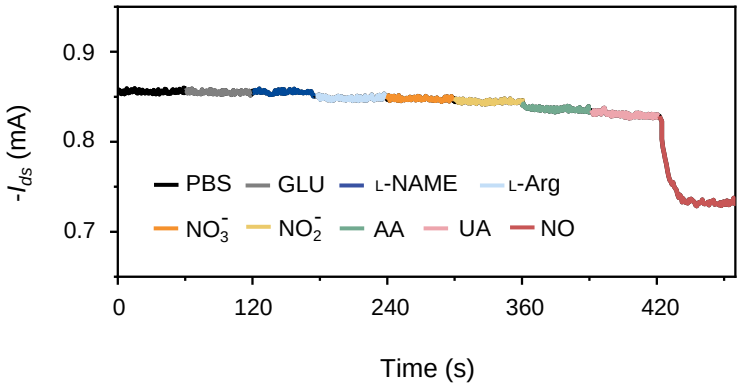

Supplementary Fig. 10: Real-time current responses of the NO sensor (I_{ds} as a function of time) with the addition of successive amounts of interfering chemicals (5 mM of L-Arg, 10 mM of L-NAME, 5 µM of other chemicals) and NO (1 µM) in PBS. The gate and drain potentials applied are 1.0 V and -0.2 V, respectively.

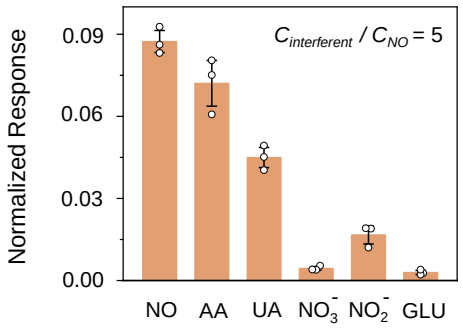

Supplementary Fig. 11: Normalized current responses of NO sensors without the modification of poly-5A1N membrane on the gate electrode, with the addition of NO (1 μM) and other potentially interfering chemicals (5 μM).

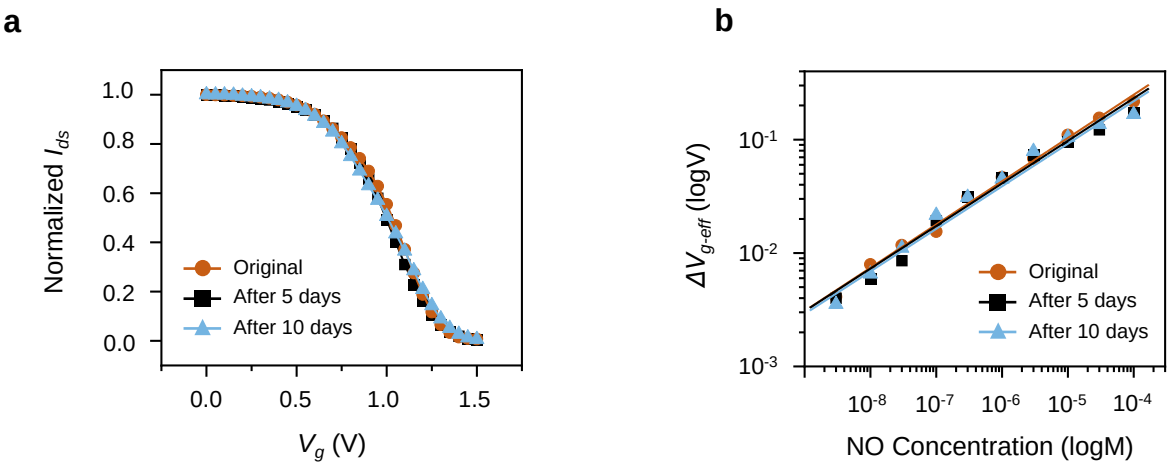

Supplementary Fig. 12: Stability tests of the NO sensor. a, Normalized transfer curves of the device after 0, 5,10 days of storage in PBS. **b,** Calibration curves of the device after 0, 5,10 days of storage in PBS.

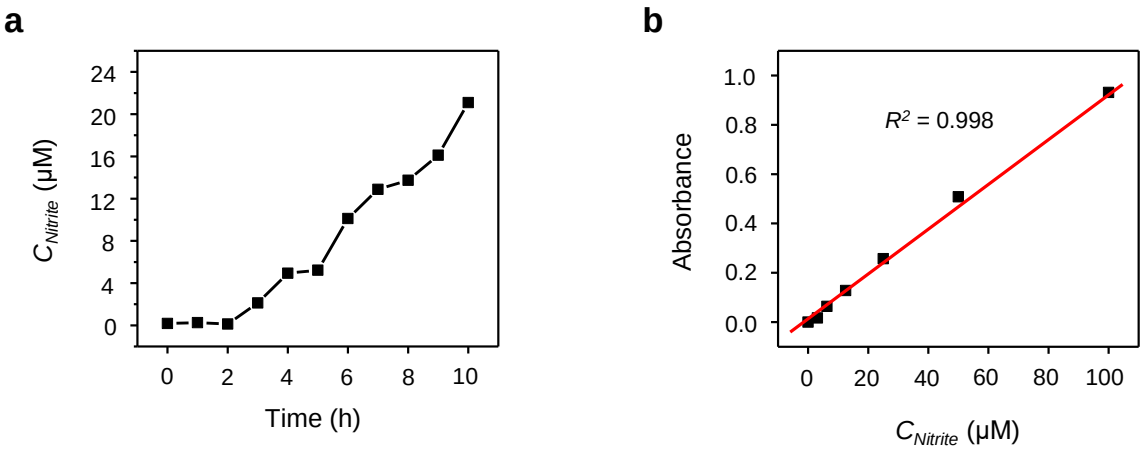

Supplementary Fig. 13: NO detection in chondrocytes cultured with IL-1b (100 µL, 10 ng mL^{-1}) by Griess test. a, Time dependent NO_2^- concentration with the addition of L-Arg (5 mM) at t = 2h. The solution is sampled every 1h. **b,** Calibration curve of Griess test. n = 3 independent experiments.

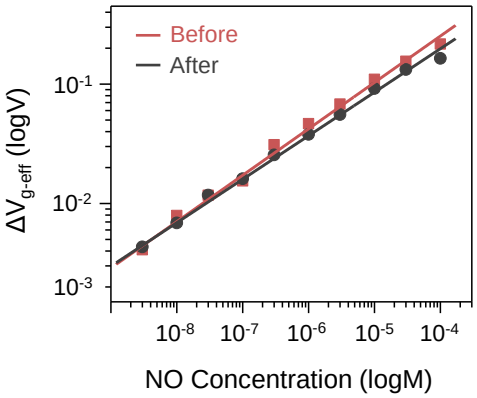

Supplementary Fig. 14: Calibration curve of the NO sensor in PBS before and after the 10-hour NO detection in chondrocytes. Red: before NO detection; Black: after NO detection.

a **b**

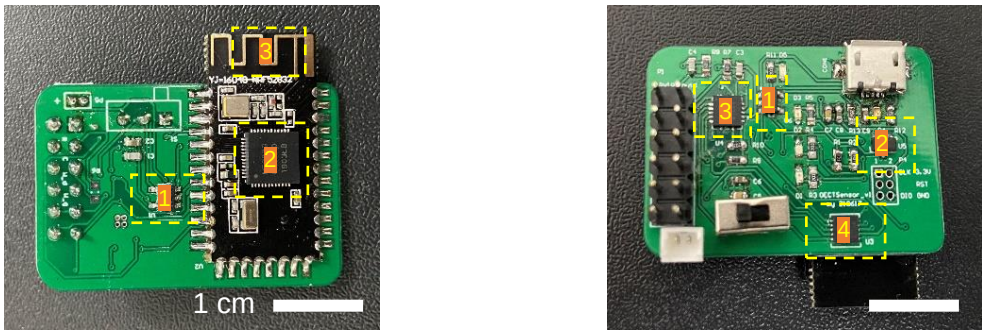

Supplementary Fig. 15: Images of the system architecture of the wireless module for the OECT-based NO sensor. a, Front side of the wireless module. 1-Battery management system (BMS); 2-Low dropout regulator (LDO); 3-Antenna. **b,** Back side of the wireless module 1-Reference; 2-Nrf52832; 3-OPA (BUFF TIAx2 AMP); 4-Digital to Analog Convertor (DAC).

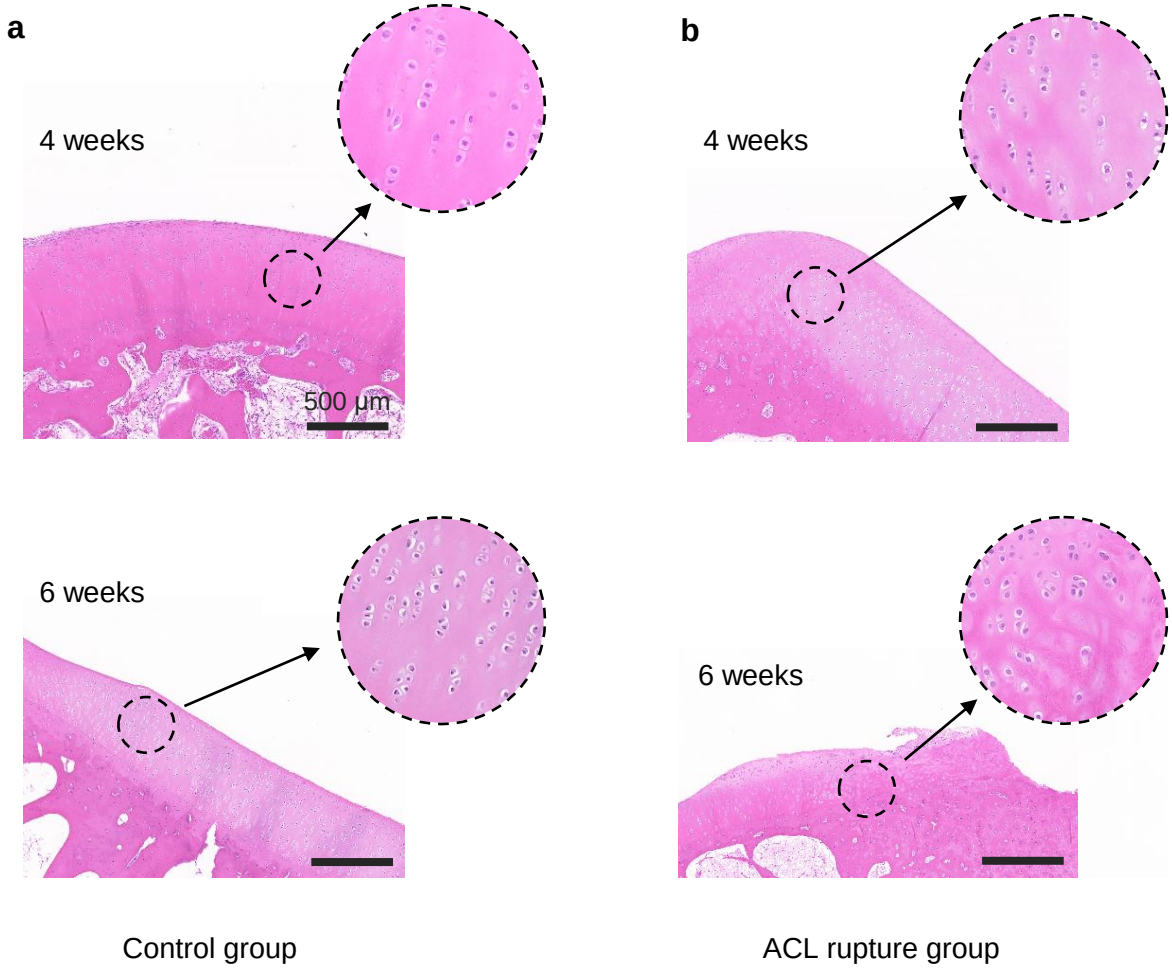

Supplementary Fig. 16: Hematoxylin–eosin (HE) staining images of the femoral condyles after 4 and 6 weeks of implantation surgeries. a, Control group. **b**, ACL rupture group.

Supplementary Table 1: Comparison of the performance of NO biosensors from the previously reported works and the current work.

Materials	Sensor configure	Sensitivity	Linear range (μM)	Detection/ Response Limit (nM)	Flexibility	Demos	in vivo test	Refs
PHF[a]/CNT /AuNPs	3-electrode	0.024 μA μM^{-1}	0.01-1	91	No	H1299 cells (30 h)	No	1
rGO/ Co_3O_4/Pt	3-electrode	0.026 μA μM^{-1}	10-650	1730	No	NO solution	No	2
GC[b]/SWNT/ PVP-OS–EA[c]	3-electrode	0.167 μA μM^{-1}	0.2-40	50	No	NO solution	No	3
Hemin/CNT/ Chitosan	3-electrode	0.002 μA μM^{-1}	0.25-1	25	No	Rat brain (~10 s)	Yes	4
Au/ Poly(eugenol)	3-electrode	0.005 μA μM^{-1} (0.01-5 μM) 0.004 μA μM^{-1} (0.01-5 μM)	0.01-100	3.97	Yes	Chondrocytes (24 h) Organs (120 s) Joint cavity (5 days)	Yes	5
GaAs/hemin	FET	-	-	1000	No	NO solution	No	6
Graphene/ hemin	FET	54 μS μM^{-1}	0.001-1	0.3	No	macrophage cells (20 h) HUVECs[d] (1200 s)	No	7
PEDOT:PSS	OECTs	94 mV dec^{-1} (~174 μA μM^{-1} or 789 μS μM^{-1} in the range of 0-1 μM)	0.003-100	3	Yes	Chondrocytes (10 h) Articular cavity (8 days)	Yes	This work

a. PHF: polysulfone hollow fiber, **b.** GC: glassy carbon, **c.** PVP-OS–EA: poly(4-vinylpyridine) (PVP) partially quaternized with 2-bromoethylamine (EA) functionalities. **d.** HUVECs: human umbilical vein ECs

References:

[1] Jiang, M. et al. A cellular nitric oxide sensor based on porous hollow fiber with flow-through configuration. *Biosensors and Bioelectronics* **191**, 113442 (2021).

[2] Shahid, M.M. et al. An electrochemical sensing platform based on a reduced graphene oxide–cobalt oxide nanocube@platinum nanocomposite for nitric oxide detection. *Journal of Materials Chemistry A* **3**, 14458-14468 (2015).

[3] Fei, J., Hu, S. & Shiu, K.-K. Amperometric determination of nitric oxide at a carbon nanotube modified electrode with redox polymer coating. *Journal of Solid State Electrochemistry* **15**, 519-523 (2011).

[4] Santos, R.M., Rodrigues, M.S., Laranjinha, J. & Barbosa, R.M. Biomimetic sensor based on hemin/carbon nanotubes/chitosan modified microelectrode for nitric oxide measurement in the brain. *Biosensors and Bioelectronics* **44**, 152-159 (2013).

[5] Li, R. et al. A flexible and physically transient electrochemical sensor for real-time wireless nitric oxide monitoring. *Nature Communications* **11**, 3207 (2020).

[6] Wu, D.G. et al. Direct Detection of Low-Concentration NO in Physiological Solutions by a New GaAs-Based Sensor. *Chemistry – A European Journal* **7**, 1743-1749 (2001).

[7] Jiang, S. et al. Real-time electrical detection of nitric oxide in biological systems with sub-nanomolar sensitivity. *Nature Communications* **4**, 2225 (2013).

Supplementary Movie 1: Wireless module for remotely measuring the transfer curves of NO sensors and the channel current response with the addition of NO solutions, with data transmitted to a mobile device.